This is to certify that the

dissertation entitled

REMOTE SENSING OF WHOLE-FIELD FLOW RATES
OF GLACIERS AND OTHER LARGE BODIES
USING INTERFEROMETRIC METHODS

presented by

EDGAR GEORGE CONLEY

has been accepted towards fulfillment
of the requirements for

Ph. D. degree in APPLIED MECHANICS

Gary Lee Cloud
Major professor

GARY LEE CLOUD

Date 23 July 1986

REMOTE SENSING OF WHOLE-FIELD FLOW RATES OF GLACIERS AND OTHER LARGE BODIES USING INTERFEROMETRIC METHODS

By

Edgar George Conley

A DISSERTATION

Submitted to
Michigan State University
in partial fulfillment of the requirements
for the degree of

DOCTOR OF PHILOSOPHY

Department of Metallurgy, Mechanics and Materials Science

1986

The
ligh
doub
phot
the
pair
resu
spac
phot
non-
patt
imag
duri
non-

This
ligh
Glac
Nonc
are
meth

ABSTRACT

REMOTE SENSING OF WHOLE-FIELD FLOW RATES
OF GLACIERS AND OTHER LARGE BODIES
USING INTERFEROMETRIC METHODS

By

Edgar George Conley

The flow of glacier ice is mapped using noncoherent (white) light speckle interferometry. Time-lapse, high resolution, double exposure of a sun-illuminated glacier surface yields photographic transparencies which diffract coherent light in the manner of Young's experiment. In Young's experiment, a pair of knife-edge slits diffract light such that the resulting interference fringe patterns are indicative of the spacing between the slits. Such slits may be generated photographically simply by imaging shadows appearing on a non-coherently illuminated, optically rough surface. Fringe patterns arising from the double exposed glacier surface image yield information about ice displacement taking place during the exposure interval. The method is non-contacting, non-invasive and whole-field.

This thesis describes experimental application of the white light speckle method to the surfaces of both the Nisqually Glacier, WA and to the Ptarmigan Glacier, Juneau, AK. Noncoherent imaging and coherent optical processing theory are presented along with experimental and data analysis methods.

Lim
imp
occ
mir
'fr
the

The
flo
whe
the
mac
pe
da

Go
te
sp
se
an

Limitations on applicability, resolution and accuracy are imposed by weather, atmospheric turbidity and camera motion occurring between exposures. Weather problems can be minimized by proper choice of field season. Methods to 'freeze' atmospheric turbulence and to gauge the motion of the camera are proposed.

The results from the field seasons are consistent with the flow-rates collected by conventional means at the Nisqually, whereas poor weather ruined results at the Ptarmigan. On the limited areas of overlap for which comparison can be made, this method yields surface flow rates of 0.6 meters per day while surveying methods yield about 0.4 meters per day.

Good agreement with the results of traditional measurement techniques suggests other applications of the white light speckle method. These include, determination of river and sea-ice flow, mine wall strains, volcanic slope stability, and possibly, tectonic plate strains.

The
sci
kno
by
Gar
yea

I a
T.
con

Fir
Er
of

ACKNOWLEDGEMENT

The greatest debt owed by an author is to the many scientists who took the time and effort to write down their knowledge. I thank them. The greatest personal debt owed by this author is to my advisor and confidant, Professor Gary Cloud. I wish to express my appreciation for his many years of unfailing assistance and encouragement.

I am also grateful to advisory committee members Professors T. H. Edwards, J. F. Martin and H. F. Bennett whose care and concern, on my behalf, was obvious.

Finally, I acknowledge the patience and dedication of Mr. Eric Burgoon who, during the early stages of the research, offered invaluable assistance in both field and laboratory.

TABLE OF CONTENTS

4. DISCUSSION AND CONCLUSIONS

APPENDICES

LIST OF TABLES

LIST OF FIGURES

CHAPTER 1

CHAPTER 2

CHAPTER 3

CHAPTER 4

CHAPTER 1

INTRODUCTION

I. THE GEOPHYSICAL MEASUREMENT PROBLEM

Fundamental principles of mechanics have, in the past three decades, been applied to the study of motion of tectonic plates, to the stability of volcanic slopes, to the flow of ice and it's interaction with surroundings, and to other naturally occurring systems. Theories of rheology, mass transport, and heat transfer are being related to knowledge gained through observation. Physical principles are insufficient to render a tractable set of equations: Phenomenological relations are required. Since metrology is the principal means of gathering the required facts, accurate experimental determination of boundary conditions is essential. Such information is needed to guide the thinking of theoreticians, as well as to check the predictions of their models.

Major components of the boundary set of geophysical processes are surface velocity and strain rate maps. Geophysical systems, however, pose a singular problem in measurement. Very long time scales and distances (i.e. gage lengths) are inherent in traditional methods. Measuring techniques, in general, locate objects or distinctive

features in the the field of interest relative to one another or to some fixed point by surveying, photogrammetry, taping, etc. Large systems require extensive grids of either natural or artificial markers, while instruments and methods must yield displacements of these features accurate to better than one percent. The North American continent, for example, drifts west about .1 meter per year [1] and measures roughly 5000 kilometers from coast to coast. Determination of annual continental strain rates requires a technique accurate to about 1 part in 50 million. Such accuracy exceeds the limits of standard measurement strategy.

Accuracy is also eroded by certain common analysis techniques. Average velocity of a glacier surface feature, for example, is calculated by dividing the distance the feature has traveled by the elapsed time. This value is assigned to the point mid-way between the feature's initial and final positions. Rasmussen [2] has pointed out that, "The average velocity does not occur at the mid-point...unless the actual velocity distribution belongs to a restricted class of mathematical functions". Errors amounting to several percent can result.

In addition to accuracy limitations, mechanicians also note the conflict between Eulerian (spatial) and Lagrangian (material) coordinates systems inherent with long time

scales and gage lengths. An Eulerian system should be used since strain is a function of both time and space. Long time scales, required to obtain meaningful readings, result in the gross movement of the gage site which obscures the Eulerian character of the flow. The Lagrangian view, which devotes attention to a single particle flowing in the system of interest, is most often used in the analysis of fluid flow. Long gage lengths, which cannot account for strain gradients within a gage site, obscure Lagrangian depiction. Thus, efforts devoted to field strain rate measurement of many important geophysical processes were frustrated, and new methods were called for. Noted glaciologist W. S. B. Patterson [34], in 1969, wrote, "...now the prime need is for more, or rather better, data."

II. HISTORICAL BACKGROUND - SPECKLE INTERFEROMETRY

Experimentalists required a simple technique having short gage lengths and time scales which yields whole-field maps of surface strain rates and velocities. Noncoherent (white) light speckle interferometry is such a technique. This optical method is an offshoot of the new, but well understood, methods of holographic interferometry. Five important developments are relative to the maturation and application of the method:

A. Young's experiment

In 1889, English physician Thomas Young discovered that a pair of closely spaced knife-edge slits, when illuminated by nearly coherent light, gives fringes which are indicative of the spacing and orientation of the slits as in Figure 1.1. The distance between the slits is approximated by the relation

$$d = \frac{\lambda L}{S}, \qquad \text{for } d \gg \lambda \qquad (1.1)$$

where d is the distance between the slits, λ is the wavelength of the slit illuminating coherent light, L is the distance between the plane of the slits and the observation screen (on which the fringe patterns are viewed) and S is the separation between adjacent fringe axes. (Derivation of this formula is given in Chapter 3.)

B. The laser speckle phenomenon

The speckle effect, visible when coherent (laser) light impinges on a surface, was considered a nuisance during the first experiments in holographic interferometry. Coherent light, reflected from a surface with inherent natural roughness, recombines at the eye to form bright 'speckle cells', covering about 5% [9] of a dark background. This

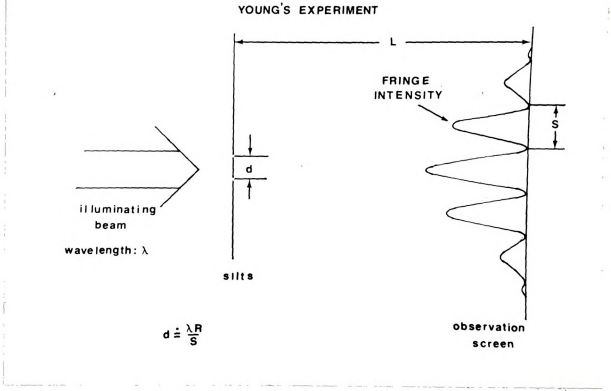

Figure 1.1 Young's experiment

random interference, which causes optical 'noise' in holography is, nevertheless, uniquely characteristic of the illuminated surface; if the surface moves, so does the intact pattern of speckles. High resolution, double photographic exposures of such a surface, taken before and after small, uniform in-plane displacement of the surface, renders rows of equally sheared speckle patterns appearing in the processed image. When viewed under the microscope, such an image has a distinctive 'corn-row' pinhole appearance as shown in Figure 1.2 (reproduced from Cloud [63]), first noticed by Burch and Tokarski [3]. As reported in their landmark paper, these workers photographically produced a multiple pinhole image structure which acted as a diffraction grating. Such a grating diffracts coherent light in the same manner as Young's optical slits. Referred to the film plane, the object displacement between exposures is thus given by eqn. (1.1).

C. The laser speckle method applied to displacement and strain measurement

Merging the ideas in the last two paragraphs, Archbold, Burch and Ennos [4], applied the laser speckle method to surface displacement analysis. If photographic resolution is sufficiently high, if the speckle cells are 'contrasty', and if displacement is neither too large nor too small, Young's fringes result if the double exposed, processed

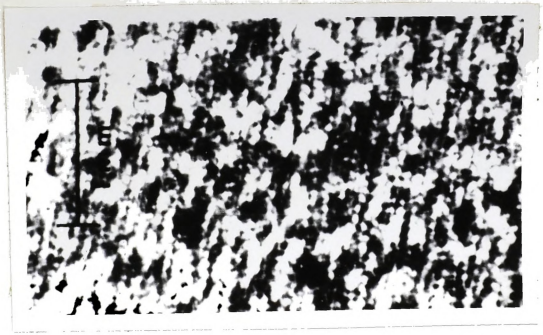

Figure 1.2 Speckle pattern micrograph (from Cloud [63])

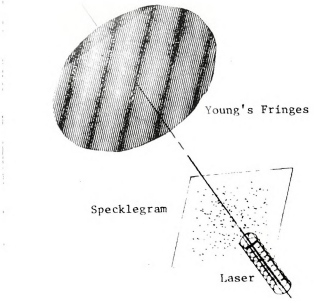

Figure 1.3 Young's Fringes generated from specklegram

photograph (specklegram) is interrogated with a narrow beam of coherent light as in Young's experiment, Figure 1.3. (Range of useful sensitivity is discussed in the following chapter.) Furthermore, the fringe patterns will be indicative of the displacement vector, which is perpendicular to the fringe axis, in the plane of the film, according to eqn. (1.1). In a practical application of Archbold's experiment, Cloud [5] has successfully gaged the rotation of an aluminum disk using the laser speckle technique.

D. The white light speckle method

In a critical development, Boone and DeBacker [11], in 1975, applied the speckle method to a specially prepared retroreflective surface which was illuminated by noncoherent (white) light. Extending this idea, Boone and DeBacker also reported the requisite speckle structure also appeared in the photographic image when the light source is placed to emphasize natural surface roughness. In their experiments, a concrete beam (presumably not polished) was illuminated with an ordinary 250w lamp placed close to the plane of the surface. Thus, interference, as in laser speckle, was not necessary for the production of speckle cells. Geometric shadows appearing on the object surface suffice. Illumination with a (relatively expensive) coherent source

and special surface preparation was avoided, paving the way for many new applications.

Other investigators quickly followed, reporting novel applications and extensions of the new method. In 1975, Burch and Forno [12] reported success using the same ideas and 'tuned' apertures. Special masks fitted to the recording camera lens selected specific frequency bands and preferred displacement directions, thereby filtering unwanted frequencies and noise from the optical signal before photographic recording. Maddux [14], in 1975, reported on an automated digital data acquisition system which logs fringe pattern information using diode arrays and computing machines. In a biomedical application, Cloud [15] applied the white light method to strains in skin in vivo. Except for the work of this laboratory [59] [60] [61] [62], little practical application of the method outside of the laboratory has been reported.

E. Merging problem and solution

Applications of optical metrology offered in the literature as illustrations of a new theory or technique are usually experiments using engineering materials which measure less than 1 meter in length. This is understandable since these objects are easily handled in machine shop and laboratory. Hence mechanicians, expecially experimentalists, can become

'stuck' thinking small. Geologists, on the other hand, accustomed to working with bodies many kilometers in size would not be given to inquire of the latest techniques to detect displacements on the order of the wavelength of visible light in 'typical' engineering materials such as steel, aluminum or composites.

In 1978, Cloud [5], [15] noted that the texture of ice (appearing in a photograph) of an Alaskan glacier seemed to have the prescribed roughness which made Boone and DeBacker's experiment successful. Glaciers are heavily marked by surface undulations, crevasses, suncups, windborne dust, moraine (till) and other materials. Cloud speculated that such large and small scale random patterns could be utilized to generate the speckle effect and proposed to the National Science Foundation [16] a study of the feasibility of applying the white light speckle method to glaciers and to other dynamic geological systems. For the first time, powerful, new interferometric techniques were brought to bear upon large, naturally occurring surfaces.

III. APPLICATION TO GLACIERS

A. Glacier study

Among the reasons to study glaciers is that glaciers move. Movement, amounting to roughly 1 meter per day [17], is relatively fast compared with other geophysical processes and so provides 'quick' verifications of new methods in large scale metrology and flow theories. Glaciers thus provide a convenient proving ground for basic concepts regarding metamorphic flow of rock within the earth. Justification lies partly in the fact that rock, as well as ice, is a polycrystalline substance and should deform in similar ways [18]. Theories of plate tectonics, according to Weertman [19], face crucial tests in the interiors of glaciers. Glacier flow, on a smaller scale, mimics the behavior of large ice sheets. An understanding of these bodies is important since large scale changes in polar ice, for example, affect world climate and sea level. Thus, recent theories of glacier mechanics may have application beyond the immediate goal.

In addition to yielding understanding of basic geology, the study of glacier flow deserves special attention. Glaciers are an important shaper of topography in the form of erosion and deposition [40]. As world population expands, and more demand is placed upon natural resources, geologists will

require detailed histories of the forces which shape the surface of the planet in order to exploit these resources. Glacier regions, for example, form important hydrological power sources in the Netherlands [21] and elsewhere in Europe [22]. Understanding of glacial mass balance is necessary to provide for the increased electrical demands of these areas.

Glaciers also provide a sensitive climatological indicator [23]. Now, glaciers cover about 10% of the earth's surface. Siberia, Europe and most of North America were cloaked during the last ice age [26] but despite much work, dramatic, sudden growth of ice sheets remains unexplained. Understanding the growth of large ice masses requires sophisticated appreciation of long and short term dynamical processes. Detailed knowledge of glacier dynamics is also critical to dating layers of ice extracted from boreholes. Pollen, oxygen, radioactivity content and other substances trapped in the ice offer clues to past climates and to predictions of possible future glacier behavior. The 'greenhouse theory', for example, may be substantiated by determining the carbon dioxide content of air bubbles trapped in ancient glacier strata.

B. Historical background-glacier flow rate measurement

As in other geophysical disciplines, the early 1950's saw the concepts of mechanics and physics applied to the glacier flow problem (e.g. [24], [25]). Accurate knowledge of flow rates was required and geologists turned to orthodox methods. The classic method of glacier surface strain measurement is to set stakes in the ice and periodically measure the distance between the stakes with tape, theodolite, photogrammetry or, more recently, electronic distance measuring devices. Strains are calculated by dividing the change of distance by the original distance between stakes. While this method is simple and straightforward, its precision is impaired by several factors. Physical access to the stake site is necessary; an obvious drawback during certain seasons on glaciers with steep icefalls. Stakes tip, melt into or out of the the ice (c.f. [43]), or become covered with snow since measurement over long time periods (perhaps years, e.g. Hodge [28]) may be required. Whole field flow or strainrate determination requires a grid of stakes covering much of the surface. Such grids are impractical to put in place and maintain except on a very small scale. Because of these pitfalls the staking method is used principally to determine centerline flow rates [28] or shear flow across selected cross sections [29].

Warner [30] and Warner and Cloud [31] have used a substantially different approach. A classic strain rosette, using wires frozen into the glacier surface yielded strainrates for a temperate valley glacier. Short gage lengths and time scales resolved the conflict between Lagrangian and Eulerian coordinate systems but the method is tedious and provides information for just one point.

IV. SUMMARY

The white light speckle method provides field workers with a simple technique having infinitely small gage lengths and relatively short time scales which yields full field maps of glacier surface flow rates. The acquisition of data requires only a perch from which to obtain high resolution photographs of the straining surface, lighting conditions emphasizing natural surface roughness and two clear periods of weather providing optical access to the subject. Glacier surface displacement rates are subsequently determined in the laboratory through coherent optical processing and comparison with topological maps.

V. ORGANIZATION OF DISSERTATION

The following chapter details the theory of data recording (imaging) and processing (filtering) supporting the interferometric speckle technique. Relevant practical

aspects of applying the noncoherent method to displacement analysis are discussed.

Chapter 3 details the feasibility of applying the technique to the surface of two temperate valley glaciers: Nisqually Glacier, Mt. Rainier National Park, WA, and the Ptarmigan Glacier, Juneau Ice Field, Juneau, AK, USA. Surface flow rates and geometry of each body are relatively well documented, allowing limited comparison of the results of the new method to the results of established techniques. This chapter recounts experimental procedures and elaborates results of field seasons 1981 and 1982. Choice of instruments and methods for the second field season were largely determined by the experience of the first year. Preserving chronological order, preliminary conclusions, based on first year experiments are given in this section.

Discussion and conclusions, error analysis, recommendations for further study and adaptation of the optical method to other measurement problems are given in the final chapter.

CHAPTER 2

THEORY OF IMAGING AND FILTERING

P.M. Duffieux, in 1946 [50], was first to suggest that Fourier methods be applied to optics. Other workers have extended this notion until, at this time, there is little distinction between the mathematics of optics and communication theory. Following these pioneers, this paper examines the imaging and filtering processes using frequency analysis.

I. IMAGING

Recent texts (c.f. [46], [47]) describe the noncoherent-light imaging process as an extension of the coherent-light process. This is the method used below. Comparisons are made, where informative, between the coherent and noncoherent cases. One-dimensional equations are used because of their relative simplicity and facility. Little generality is lost by employing one-dimensional analysis. In some circumstances, however, appeal is made to intuition by describing the equations in terms of their multi-dimensional effects.

Wave energy which is capable of interfering with itself is considered to be spatially coherent. In the first case

discussed below, the object surface is illuminated with coherent light. Such illumination, when reflected or scattered by an optically rough surface, interferes (recombines) at the eye to form a random pattern of bright points known as speckle cells. In the second case discussed below, the object surface is considered to be illuminated with noncoherent light. Noncoherent illumination is not capable of producing interference effects. The mathematics in this chapter provides theoretical basis for this behavior.

The restricted (Fraunhoffer) case is assumed throughout, where object and image points are located at very small angles from the optical axis.

A. Coherent illumination

Consider the case where an object surface is illuminated with spatially coherent light and, given the amplitude of the reflected light as a function of object plane coordinates, the corresponding amplitude distribution of the image is to be determined. Following Born and Wolf [20], major assumptions are as follows:

Coherent illumination of the object surface.

Small angles with respect to the optical axis. This is an important restriction; point sources produce spherical wavefronts. If a sufficiently small spherical portion is

viewed, however, the wavefront can be considered plane. Such a condition meets the so-called Fraunhoffer diffraction restrictions. Fraunhoffer conditions have wide application in applied optics, greatly simplifying the mathematics.

Unity magnification.

For the real images considered, the subscripts indicating object and image points indicate object-image inversion. That is, left on the object is right on the image.

Unity index of refraction

Isoplanatism, defined as the existence of a region sufficiently small such that a displacement in the object plane results in no change of shape, orientation or distortion of the image. In this region the point spread function (that is, the image of a point source) is constant as the source point explores the object surface.

Integration of complex quantities often results in a constant multiplier. Such constants, indicating phase change of a wave propagating through a lens, losses due to reflection or absorbtion or diminished intensity of spherically radiating waves, for example, are usually neglected in this type of work.

The observable or detectable quantity is intensity, defined in terms of the complex amplitude as

$$I(x) = [U(x)]^2 = U(x)\ U^*(x).$$

Recalling the properties of complex functions, squaring the complex amplitude obliterates phase information; it is unnecessary to carry such arithmetic baggage through the integration process. Thus, the expression, "...ignoring nonessential phase terms (or constants)...", is often used following an integration. The consequence is less cumbersome, and perfectly useful expressions.

Consider the case where light energy is transmitted through an aperture from object to image planes as in Figure 2.1. The nomenclature is as follows:

x_o , x_1 and σ are coordinates in the object, image and aperture planes respectively.

$U_o(x_o)$ is the complex amplitude of the light disturbance on the object plane. In this development, the notion of complex amplitude will be used. Eliminating the time dependence of the electric field vector, complex amplitude is a function of position only, thus reducing and simplifying the analysis with so-called 'scalar diffraction theory'.

$K(x_o;x_1)$ is the transmission function (also called the transmission factor or the amplitude impulse response). This function is defined as the complex amplitude of the disturbance on the image plane due to a disturbance in the

object plane which is of unit amplitude and zero phase and which extends over a unit length of the object line (in the current one-dimensional system). The general notational form, $K(x_o;x_1)$, indicates a nonlinear phase change occurring in the process of transmitting wave energy from object to image. 'Nonlinear phase change' means that the phase of a wave, propagating for example, from x_o to x_1, does not depend simply on the distance between the two points. Below, K is given a more restrictive, linear form.

$U_i(x_1)$ is the complex amplitude of the light disturbance in the image plane.

Beginning the analysis, consider the contribution of light amplitude in the image plane at location x_1 from a light disturbance originating at x_o in the object plane. The contribution is $dU_i(x_1) = U_o(x_o)\ K(x_o;x_1)\ dx_o$. The total amplitude at point x_1 is

$$U_i(x_1) = \int_{\pm\infty} U_o(x_o)\ K(x_o;x_1)\ dx_o, \qquad (2.1)$$

which is recognized as the convolution of the input amplitude with the amplitude impulse response.

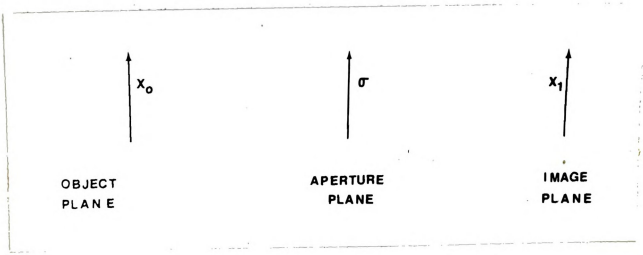

Figure 2.1 Imaging geometry

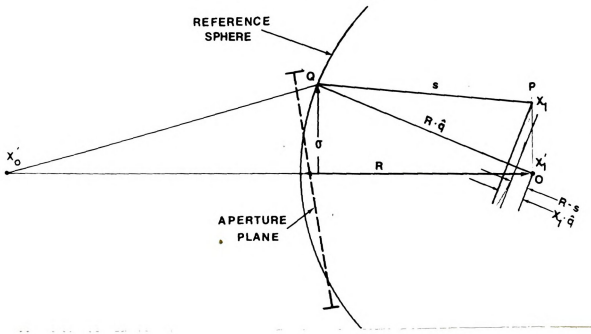

Figure 2.2 Reference sphere for circular aperture

The integral extends formally to infinity but actually extends only to the limit of the object. In the remainder of this chapter, all integrals will extend to $\pm \infty$, except where indicated. This is done, it shall be seen, to maintain the formalism of the Fourier integral.

Now the task is to generate an expression for K, the amplitude impulse response. Consider a unit source placed in the object plane at x_o', that is,

$$U_o(x_o) = \delta(x_o - x_o'),$$

where δ is the Dirac delta function. Substituting this into eqn. (2.1) and noting the sifting properties of the delta function gives

$$U_i(x_1) = K(x_o'; x_1). \qquad (2.2)$$

That is, the transmission function now represents the image plane disturbance due to a point source.

Now take a large sphere (the reference sphere) centered about a point, x_1', on the image plane as shown in Figure 2.2. For the time being, let the reference axis be $x_o' x_1'$. The classic assumption here is that such a large spherical surface (compared with the aperture), at very small angles

is a good approximation to the aperture plane. (This is the Fraunhoffer condition.) Let there be a point disturbance on the object plane and let the resulting disturbance, $H(\sigma)$, on the reference sphere (the sphere is represented by a circle in the vertical one dimensional analysis) be written as

$$H(\sigma) = G(\sigma)\frac{\exp(-\frac{2\pi iR}{\lambda})}{R} \qquad (2.3)$$

where R is the focal length of the imaging lens placed in the aperture and λ is the wavelength of the illuminating light. The phase of G is the phase aberration of the system while the amplitude of G is the amplitude distortion of the image forming wave. G is the so-called 'pupil function' and is taken to be constant inside the aperture and zero outside. Mathematically this is expressed as

$$G = 1 \quad \text{for} \quad \sigma \leq a$$
$$G = 0 \quad \text{for} \quad \sigma > a.$$

Though it is filled with a lens, the aperture is assumed 'clear' for the following reason. It is assumed that thin lenses act as light benders only. They simply affect the phase of the wave energy passing through them. As long as the energy is directed to the necessary place (i.e. the focal plane), phase information, for the present purpose, is 'nonessential'. In the absence of such a lens the focal

plane would simply be displaced to another location (i.e. at infinity).

The disturbance at point x_1 in the neighborhood of x_1' on the image plane is the sum of the contributions from each point on the reference circle which approximately fills the aperture. Using the Huygens-Fresnel principle wherein each point Q on the wavefront is considered to be the source of a new wavelet, the total disturbance on the image plane is written

$$U_i(x_1) = \int H(\sigma) \frac{\exp(\frac{2\pi i s}{\lambda})}{s} d\sigma, \qquad (2.4)$$

where s is the distance from the aperture point Q to the image plane point x_1. This simplified version of the integral theorem of Kirchhoff is the well-known Fraunhoffer equation; it is obtained when very small field angles are assumed. The integrand phase factor $\exp(2\pi i s/\lambda)$ and the factor $1/s$, (the latter diminishes amplitude with distance) occur during the propagation of a spherical wave. In Born and Wolf's rigorous derivation, the denominator s is left in the equation until it is shown to contribute only a nonessential constant. This is true only of the denominator since s, in the exponent, causes the exponential to vary rapidly over the imaging plane. Note that when the Fraunhoffer equation is again invoked in the filtering section below, the integrand denominator is ignored from the

onset. In any event, the Fraunhoffer equation states that the amplitude in the receiving plane is found simply by integrating the phase factor over the aperture (or, in the filtering stage, the integration is carried out over the area subtended by the beam).

Now substituting eqn. (2.3) into eqn. (2.4) and again ignoring constants gives

$$U_i(x_1) = \int [G(\sigma) \frac{\exp(-\frac{2\pi i R}{\lambda})}{R}] \frac{\exp(\frac{2\pi i s}{\lambda})}{s} d\sigma. \qquad (2.5)$$

Based on the geometry of Figure 2.2, it is evident that as the triangle OPQ becomes horizontally stretched, the distance (R - s) will become a very good approximation to $\mathbf{q} \cdot \mathbf{x}_1$, where $\mathbf{q}$ is the unit vector directed from O to Q, the point of disturbance on the reference sphere. (See Born and Wolf [20] for a mathematically rigorous derivation.) Thus, for small angles, $R - s \approx \mathbf{q} \cdot \mathbf{x}_1$. Rewriting and noting that in the one dimensional system, the magnitude of $\mathbf{q}$ in the direction of $\mathbf{x}_1$ is $\frac{\sigma}{R}$, thus, $s \approx R - \frac{\sigma}{R}(x_1)$.

The lateral distance from the center of the reference sphere to the neighboring image point may be represented by the distance $x_1 - x_1'$, which is approximately equal to $x_1 - x_o'$

(again for small angles), and thus, $s \approx R - \frac{\sigma}{R}(x_1 - x_o')$.

Substituting this expression for s into eqn. (2.5) gives

$$U_i(x_1) = \int G(\sigma) \frac{\exp(-\frac{2\pi i R}{\lambda}) \exp\{\frac{2\pi i}{\lambda}[R - \frac{\sigma}{R}(x_1 - x_o')]\}}{R\,[R - \frac{\sigma}{R}(x_1 - x_o')]}\, d\sigma.$$

Where $R \gg \sigma$ and $R \gg (x_1 - x_o')$, which must hold for the assumed small angles, the integrand denominator reduces to the constant R^2 (which can thus be ignored) and this gives,

$$U_i(x_1) = \int G(\sigma)\, e^{-\frac{2\pi i}{\lambda R}(x_1 - x_o')\sigma}\, d\sigma. \qquad (2.6)$$

Consider again the transmission function K. K accounts for amplitude and phase variation as light energy propagates through the optical system. If this function is sufficiently well behaved over a small region of space, it is said to be space (or shift)-invariant. That is, a small shift in object plane coordinate will result in no distortion of the image. Throughout this small region, K is linear depending only on the distance $(x_1 - x_o')$ between the object and image points. In this case, the transmission function may be written $K(x_o'; x_1) = K(x_1 - x_o')$, where K is now defined for a very small 'isoplanatic' region of the system.

Finally, comparing eqn. (2.6) with eqn. (2.2) and dropping the primes it is seen that

$$K(x_1 - x_o) = \int G(\sigma) \exp[-\frac{2\pi i}{\lambda R}(x_1 - x_o)\sigma] \, d\sigma. \qquad (2.7)$$

Thus, the amplitude impulse response of the optical system is dependent on the pupil function which is, itself, independent of the object point.

Now an arbitrary transmission function, K(x), may be expressed in terms of its Fourier Integral:

$$K(x) = \int k(u) \exp(-2\pi ixu) du, \qquad (2.8a)$$

where x is the space variable and u is the frequency variable.

Eqn. (2.8a) can be written in shorthand notation as

$$K(x) = FT^{-1}(k(u)).$$

Since K(x) and k(u) constitute a transform pair,

$$k(u) = \int K(x) \exp(2\pi iux) \, dx = FT(K(x)), \qquad (2.8b)$$

where k(u) is the frequency response. The amplitude impulse response and the frequency response are Fourier transforms of one another.

Note that if the variables are changed, letting

$$u = \sigma/\lambda R, \qquad (2.9)$$

then $du = d\sigma$, ignoring constants. Also, if $x = (x_1 - x_o)$, then eqn. (2.7) and eqn. (2.8a) are similar. Moreover,

$$k(\sigma/\lambda R) = G(\sigma), \qquad (2.10)$$

i.e. the frequency response is simply a scaled version of the pupil function.

Recalling σ is the coordinate in the aperture plane, it is seen that the maximum spatial frequency transmitted by a circular aperture of radius a, for example, is

$$u_{max} = \frac{a}{\lambda R}. \qquad (2.10a)$$

Therefore, spatial frequencies appearing on the object plane greater than u_{max} are 'clipped' in a manner similar to the action of an electronic low-pass filter and do not appear in the image.

In optical work, k(u) is known as the imaging system frequency response. The modulus of the complex function k is called the modulation transfer function (MTF).

Physically, the MTF plays the part of reducing the image contrast of the higher frequency components.

Note that eqn. (2.1) may be written in a simpler manner by using the convolution theorem (c.f. [46]) for Fourier transforms. The theorem states that the Fourier transform of the convolution of two functions is equal to the product of their individual transforms. Specifically for the present case and, using the shorthand notation,

$$FT\{U_i(x_1)\} = FT\left\{\int U_o(x_o)\, K(x_1 - x_o)\, dx_o\right\} = u_o(u)\, k(u).$$

where, $u_o(u) = FT\{U_o(x_o)\}$ and, $u_i(u) = FT\{U_i(x_1)\}$.

$$\text{Thus, } u_i(u) = u_o(u)\, k(u). \qquad (2.11)$$

This simple relation implies that the image is a superposition of space-harmonic components u_o, and that each component is weighted by the frequency response function $k(u)$.

For the present purposes there is no longer a need to consider imaging with coherent illumination. The theory is sufficiently developed to extend to the noncoherent case and to make comparisons where necessary.

B. Noncoherent illumination

Consider the case where an object surface is illuminated by light having a narrow temporal-frequency spectrum but which is spatially noncoherent. As before, the observed intensity is the quantity of interest. Again following Born and Wolf [20], and using the same assumptions as before, let $I_o(x_o)$ be the light intensity occurring over a length dx_o on the object plane. The contribution this source makes to the intensity at a point x_1 on the image plane is

$$dI_i(x_1) = I_o(x_o)[K(x_1 - x_o)]^2 dx_o, \tag{2.12}$$

where K is again the transmission function (impulse response) of the imaging system, defined in the previous section. It can be shown (c.f. [46] or [47]) that the noncoherent transmission function is directly proportional to the square of the modulus of the coherent transmission function. Thus the total intensity at point x_1 on the image plane is

$$I_i(x_1) = \int I_o(x_o)[K(x_1 - x_o)]^2 \, dx_o. \tag{2.13}$$

Certain aspects of coherent and noncoherent imaging can now be compared. Unlike the coherent impulse response, which is

in general complex valued, the noncoherent impulse response is real and non-negative. With coherent illumination, therefore, interference can occur, and the resulting image intensity will exhibit zeros where the corresponding object points are not zero. This is the speckle effect and explains why images of noncoherently lit objects do not suffer from zeros arising from interference; speckle patterns on such images are simply the result of zeros (i.e. shadows) of sufficient size appearing on the object surface.

Eqn. (2.13) is identifiable as the convolution of the object intensity distribution with the squared modulus of the transmission function. However, it may be expressed in a much simpler manner. Start by taking the Fourier transform of each factor:

$$FT\{I_i(x_1)\} = \Phi_i(u), \tag{2.14}$$

$$FT\{I_o(x_o)\} = \Phi_o(u), \tag{2.14b}$$

$$FT\{[K(x_1 - x_o)]^2\} = \exp(-2\pi i u x_o)\ FT\{[K(x_1)]^2\}$$
$$= \exp(-2\pi i u x_o)\ L(u),$$

where, in the last line, a shift in the space coordinate simply results in a linear phase shift in frequency space. Ignoring such a phase shift, the equality can be written,

$$FT\{[K(x_1 - x_o]^2\} = FT\{[K(x_1]^2\} = L(u) \qquad (2.14c)$$

As in the coherent case, the Fourier transform of the impulse response is known as the frequency response function, L(u), of the noncoherent imaging system.

Using eqn. (2.14c) and again using the convolution theorem, eqn. (2.13) may be written simply as

$$\Phi_i(u) = \Phi_o(u)\ L(u), \qquad (2.15)$$

and it is seen that the spatial frequency spectrum of the image is, as with coherent illumination, the product of the object spectrum and the frequency response function. (Compare to eqn. (2.11)).

Once again the task is to determine the form of the noncoherent transmission function, $[K(x_1)]^2$. Later, it will be shown that $FT\{[K(x_1)]^2\}$ is equal to the complex autocorrelation of k(u) where $FT\{K(x_1)\} = k(u)$.

Let P(x) and Q(x) be arbitrary complex functions and let

FT{P(x)} = p(u), and FT{Q(x)} = q(u). As a corollary of the convolution theorem it can be stated that

$$FT\{P(x)Q(x)\} = \int p(\beta)\, q(u - \beta)\, d\beta = p(u) * q(u), \quad \{2.16\}$$

where the asterisk indicates convolution and β is the shifting variable of integration. In words, the Fourier transform of a product of two functions is equal to the convolution of their individual transforms.

Continuing, let the conjugate of the complex function $Q(x) = P^*(x)$. Then from the properties of complex functions, $FT\{P^*(x)\} = p^*(-u)$. Thus, using {2.16}, $FT\{P(x)\, P^*(x)\} = p(u) * p^*(-u)$.

Also, using the definition of convolution and using μ as the dummy variable,

$$p(u) * p^*(-u) = \int p(\mu)\, p^*(-(u - \mu))\, d\mu = \int p(\mu)\, p^*(\mu - u) d\mu.$$

The right hand term in the above expression is the formal definition of complex autocorrelation of p(u). In this thesis complex autocorrelation will be abbreviated,

$$p(u) \odot p^*(u).$$

Autocorrelation is often encountered in optics work, and indeed occurs in the following section on filtering.

Summarizing the results, and using shorthand notation, from eqn. (2.14c),

$$FT\{[K(x)]^2\} = L(u) = k(u) \odot k^*(u). \tag{2.17}$$

Repeating eqn. (2.9), $u = \frac{\sigma}{\lambda R}$, recall λ is the wavelength of the illuminating source. In the case of noncoherent illumination, λ can be considered to be the average wavelength if the bandwidth $\Delta\lambda$, centered about λ, meets the restriction, $\lambda >> \Delta\lambda$. Since this is true (c.f. [20] or [46]) in the visible light range, in the remainder of this (imaging) section λ indicates the average illuminating wavelength. Thus from eqn. (2.10), eqn. (2.17) can be written as,

$$L(\frac{\sigma}{\lambda R}) = G(\sigma) \odot G^*(\sigma), \tag{2.18}$$

where G is again the zero-one pupil function defined on the seventh page of this chapter. In words, the noncoherent frequency response function is given by the complex autocorrelation of the aperture stop.

For a circular aperture of radius a, the autocorrelation of the pupil function can be visualized by the area common to two identical displaced circles as in Figure 2.3a. The normalized frequency response is plotted in Figure 2.3b where it is evident that the higher frequencies are imaged at reduced contrast. Khetan and Chiang [13] perform this integration (autocorrelation) and give the imaging system normalized frequency response function as

$$L(u) = [\cos^{-1}(\rho) - \rho(1 - \rho)^{1/2}], \qquad (2.18a)$$

where $\rho = u\lambda R/2a$, is the normalized position in the frequency domain. It is evident from Figure 2.3a that when the circles are displaced by 2a the frequency response function is zero. Thus, object spatial frequencies greater than

$$u_{max} = \frac{2a}{\lambda R}, \qquad (2.18b)$$

cannot appear in the image. Note that u_{max}, the maximum spatial frequency that appears in the image for coherent illumination (see eqn. (2.10a)), is exactly 1/2 of that for the noncoherent case.

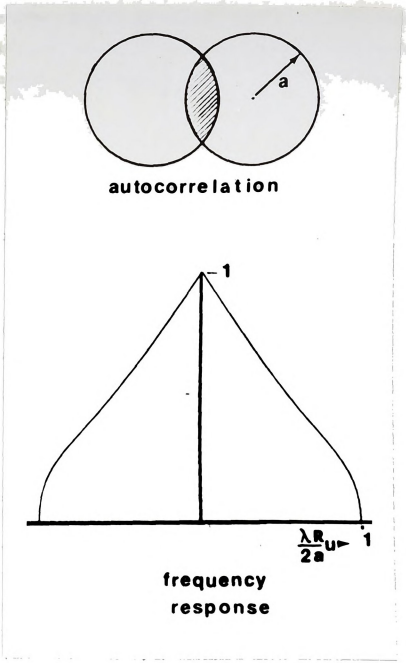

Figure 2.3a Top - Geometric interpretation of aperture function

Figure 2.3b Bottom - Autocorrelation for circular aperture

Noncoherent imaging is summarized by substituting eqn. (2.18) into eqn. (2.15) and then taking the inverse Fourier transform of each side,

$$I_i(x_1) = FT^{-1}\{\Phi_o(\frac{\sigma}{\lambda R})[G(\sigma) \odot G^*(\sigma)]\}. \qquad (2.19)$$

For a lossless system (i.e. no absorbtion or reflection), eqn. (2.19) gives the noncoherent-illumination image intensity.

C. The effect of aberrations

Goodman [47] has shown that, in general, minimum attenuation will occur with no aberrations and that their presence will decrease the image intensity to varying degrees. (For a complete review, see Born and Wolf [20] or Welford [37].) In the brief discussion on aberrations which follows, the effect of defocus is presented. Defocus is the principal, correctable problem of a quality camera system typically used for speckle interferometry. For well corrected systems, aberrations such as chromatic, spherical and astigmatic, for example, are presumed less significant and certainly less amenable to correcting from the view of an interferometrician.

In the presence of aberrations, the pupil function will take the form

$$G'(\sigma) = G(\sigma) \exp[\frac{2\pi i}{\lambda} W(\sigma)],$$

where $W(\sigma)$ is the wavefront aberration. The phase advance, $W(\sigma)$, expresses the deviation from the ideal spherical wavefront shape launched from the aperture plane. As before, the noncoherent transfer function will be the complex autocorrelation of the pupil function but the computation will not be straightforward (compared, for example, with the geometrical interpretation shown in Figure 2.3a).

Born and Wolf's [20] 'displacement theorem' (see also Welford [37]) establishes that a small change, z, along the optical axis from the ideal focal length of the receiving plane results in no change in the intensity distribution. From this and geometry they develop the simple relation,

$$W(\sigma) = 1/2(\frac{\sigma}{R})^2 z,$$

as the phase change of the wave being received at the new, defocused location.

Thus, if the amplitude is constant over the aperture plane (which is the usual assumption), the pupil function is

$$G'(\sigma) = G(\sigma) \exp[\frac{\pi i}{\lambda}(\frac{\sigma}{R})^2 z].$$

Born and Wolf [20] have performed the autocorrelation of the circular pupil function of a system suffering small amounts of defocus. Figure 2.4, showing image plane intensity distribution, is abstracted from their results. The number next to each curve is the value of the parameter,

$$m = \frac{\pi}{2\lambda} (\frac{a}{R})^2 z,$$

where z is the amount of defocus. For values of m greater than one, it can be seen that the frequency response function rapidly deteriorates at higher frequencies. For typical camera settings used in the year-two study, this equation implies z must be held to less that 0.4mm.

II. FILTERING

Speckle interferometry delineates displacements from a double-exposed photographic image of the displaced object. Assume the first image is recorded before displacement d, in the one-dimensional object space, and the second image is recorded after displacement. Also, assuming unit

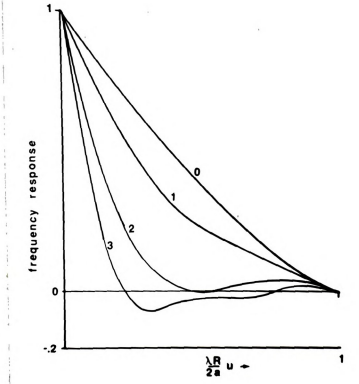

Figure 2.4 Autocorrelation for circular aperture with small defocus

magnification and photographic resolution is sufficient to record the finest object detail, the total exposure is $E(x) = [I(x) + I(x + d)]t$, where $I(x)$ is the image intensity (the subscripts from the previous section have been dropped) and t is the exposure time, assumed equal for each exposure.

Following Burch and Tokarski [3] and occasionally Khetan and Chiang [13], the amplitude transmission for a linearly developed negative film is

$$A(x) = b - ct[I(x) + I(x + d)] \qquad (2.20),$$

with b and c constants.

In the filtering process, the processed negative (specklegram) is interrogated by a narrow beam of coherent light as in Figure 2.5, detailed from Figure 1.3. If d is not too small or too large (as explained at the end of this section), Young's fringe patterns will appear on the observation screen. Such a screen may be called the transform plane, according to the following theory.

Pertaining to Figure 2.5, the nomenclature is as follows:

x is a point inside the illuminated area of the specklegram,

s is a distance on the transform plane measured from the center of the illuminating beam,

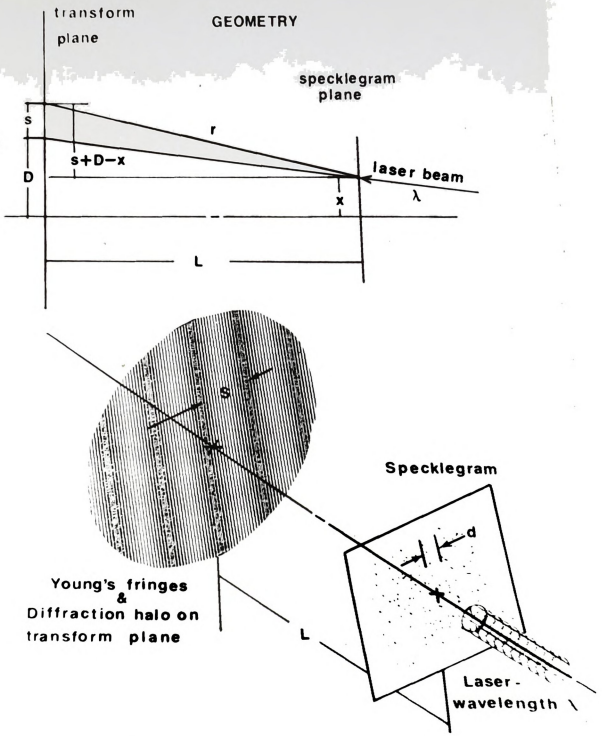

Figure 2.5 Filtering geometry

r is the distance between x and s, and

D locates the centerline of the illuminating beam.

From geometry, $r = [L^2 + (s - (x - D))^2]^{1/2}$.

When L >> s and L >> x then a good approximation is,

$$r \approx L + \frac{s^2 + 2sD}{2L} + \frac{(x - D)^2}{2L} - \frac{sx}{L}, \qquad (2.21)$$

using the first two terms of the binomial theorem.

Referring to Figure 2.5, the complex amplitude of the diffraction spectrum in the far-field region is given once again by the Fraunhoffer equation (c.f. [20] or [48]):

$$U_t(s) = C \int_{\infty} A(x) \exp(-\frac{2\pi i}{\lambda} r)\, dx.$$

Here, $U_t(s)$ is the complex amplitude in the transform plane, A(x) is the amplitude transmittance of the specklegram, C is a constant indicating nonessential phase terms, and the distance r is explained above. Cast in this form, it can be seen that the distribution of the diffracted light in the transform plane is directly proportional to the Fourier

transform of the input signal amplitude. Since $[U_t(s)]^2 = I_t(s)$, the transform plane intensity is

$$I_t(s) = [C \int A(x) \exp(-\frac{2\pi i}{\lambda} r)\, dx]^2, \qquad (2.22)$$

where the integral formally extends to infinity but actually includes only the interrogating beam width.

Consider again eqn. (2.21). Note that the first two terms are not functions of x; they contribute only to a phase change in the wavefront intercepting the transform plane, and may, therefore, be ignored. Also, for small angles, except near the center of the illuminating beam,

$$\frac{(x - D)^2}{2L} << \mathrm{ABS}(-\frac{sx}{L}), \text{ thus, } r \approx -\frac{sx}{L}.$$

Conceivably, for very small values of s, this inequality would not be true. As will be seen below, however, the transform plane intensity expression contains a singularity at s = 0 and is not valid at this point. The above approximation for r holds, therefore, because very small values of s are excluded.

It is convenient to change variables at this point. Let

$$w = \frac{s}{\lambda L} . \qquad (2.22a)$$

Now, using both the approximation for r and eqn. (2.22a), eqn. (2.22) reduces to,

$$I_t(w) = [\int A(x) \exp(2\pi i w x) \, dx]^2, \qquad (2.23a)$$

ignoring constants.

Using the Fourier transform shorthand notation, defined in this (filtering) section for an arbitrary function a, as

$$a(w) = FT\{A(x)\} = \int A(x) \exp(2\pi i w x) \, dx \qquad (2.23b)$$

and

$$A(x) = FT^{-1}\{a(w)\} = \int a(w) \exp(-2\pi i x w) \, dw, \qquad (2.23c),$$

and substituting eqn. (2.20) into eqn. (2.23a) gives

$$I_t(w) = [FT\{b - ct(I(x) + I(x + d))\}]^2. \qquad (2.23d)$$

Consider the term I(x + d). As in the imaging process, a shift in cartesian space results only in a phase shift in frequency space, with the frequency function remaining unchanged (c.f. eqn. (2.14c)). That is,

$$FT\{I(x + d)\} = \exp(2\pi iwd)\ FT\{I(x)\}.$$

Thus, eqn. (2.23d) becomes

$$I_t(w) = \{b\delta(w) - ct[FT\{I(x)\}][1 + \exp(2\pi iwd)]\}^2, \quad (2.24)$$

where the Fourier transform of a constant b is the scaled Dirac delta function.

Ignoring the δ function term, which represents the bright spot on the transform plane where $w = s = 0$, gives the transform plane intensity as

$$I_t(w) = [FT\{I(x)\}]^2[1 + \exp(2\pi iwd)]^2. \quad (2.25)$$

Before considering eqn. (2.25) quantitatively, a brief, qualitative discussion of each factor may prove helpful. It will be found that the factor $[FT\{I(x)\}]^2$, represents a circular area of random patches surrounding a central bright spot on the transform plane. Such an area is called the diffraction halo; it's size will be shown to depend on the spatial frequency of specklegram area subtended by the interrogating beam. The factor $[1 + \exp(2\pi iwd)]^2$, acts to modulate the diffraction halo rendering a set of Young's

interference fringes which are indicative of the displacement vector d.

Consider the factor $[FT(I(x))]^2$. Since amplitude squared is intensity, and using the convolution theorem,

$$[FT(I(x))]^2 = [FT([U(x)]^2)]^2 = [u(w) \odot u^*(w)]^2, \qquad (2.26)$$

where $FT[U(x)] = u(w)$. In words, the autocorrelation of the geometric aperture is the spatial frequency content of the specklegram image.

To get an idea of the transform plane intensity (that is, the diameter of the diffraction halo), a spatial frequency function, u(w), must be assumed. Burch and Tokarski [3], assumed that an ideal specklegram diffuser would contain spatial frequencies up to a certain maximum. They reasoned that the frequency content would be relatively constant near zero and fall off rapidly near w_{max}. Their normalized, ideal diffuser thus takes the shape (in frequency space) of a rectangle function, symmetric about the origin as shown in Figure 2.6.

Complex autocorrelation of the rectangular frequency distribution gives the triangular region so labelled in Figure 2.6. Light intensity distribution is the square of

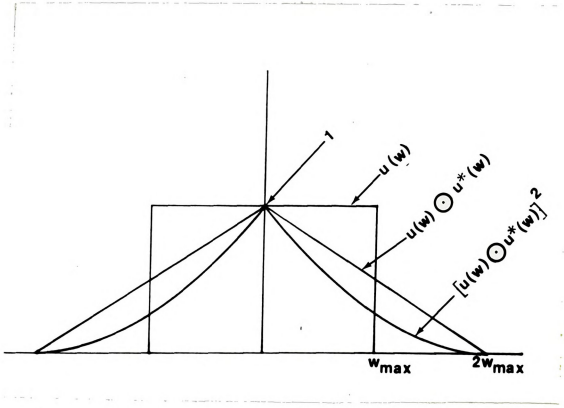

Figure 2.6 Ideal rectangular frequency function, its auto-correlation and squared autocorrelation

the autocorrelation and is also plotted in Figure 2.6. Clearly, the diffraction halo intensity drops off rapidly with increasing frequency. Indeed, most of the light energy is concentrated in the middle of the diffraction pattern between the limits $\pm w_{max}$.

It may be seen in Figure 2.6 that the extent of the diffraction halo in the transform plane is proportional to twice the maximum spatial frequency contained in the specklegram image. That is,

$$w_{max} = \frac{s_{max}}{2\lambda L}. \qquad (2.26b)$$

Use of this formula will be made in the following chapter when the spatial frequency of specklegram images are inferred from the size of the transform plane diffraction pattern.

Further explanation of the extent of the halo is given by Huygens. A beam of light impinging on a series of optical slits is deviated from its path at an angle proportional to the spatial frequency of the slits. Thus, the finer the pitch of the specklegram image, the greater the angle, and the larger the halo diameter.

Consider the second factor of eqn. (2.25),

$[1 + \exp(2\pi i w d)]^2$. Making the Euler substitution,

$$\exp(2\pi i w d) = \cos(2\pi w d) + i \sin(2\pi w d),$$

and squaring, it is found that

$$[1 + \exp(2\pi i w d)]^2 = 2[1 + \cos(2\pi w d)]$$

$$= 4 \cos^2(\pi w d), \qquad (2.27)$$

using the trigonometric identity for cosine squared.

Eqn. (2.27) has the usual zeros when,

$$wd = (n + 1/2), \quad \text{with} \quad n = \pm 0, 1, 2, \ldots \qquad (2.28)$$

Young's fringes, appearing in the diffraction halo, will have minima where

$$s = (n + 1/2) \frac{\lambda L}{d}, \quad \text{with } n = \pm 0, 1, 2, \ldots \qquad (2.29)$$

The spacing or separation, S, between adjacent fringe 'axes' is typically

$$S = s\big]_{n+1} - s\big]_n =$$

$$([(n + 1) + 1/2] - [n + 1/2])\frac{\lambda L}{d},$$

which reduces to $S = \frac{\lambda L}{d}$. Restating, the film plane displacement occurring between exposures is

$$d = \frac{\lambda L}{S},$$

which is exactly equation (1.1), mentioned in Chapter 1 in relation to Young's experiment. This remarkably simple result is critical to the success of speckle interferometric methods.

Substituting eqn. (2.27) into eqn. (2.25), and ignoring constants, gives finally the transform plane intensity as a function of image intensity and speckle shear (film-plane displacement):

$$I_t(w) = [FT(I(x))]^2 \cos^2(\pi w d). \qquad (2.30)$$

III. SUMMARY OF IMAGING AND FILTERING RESULTS

From the first section (Chapter 2.I.B), repeating the noncoherent case, image intensity is

$$I(x) = FT^{-1}\{\Phi_o(\frac{\sigma}{\lambda_n R})[G(\sigma) \odot G^*(\sigma)]\}, \qquad (2.19)$$

where the subscripts on I and x, indicating image plane coordinates, have been dropped. Now, the object illuminating, noncoherent, average wavelength λ_n, is distinguished from the coherent, filtering beam wavelength, λ_c.

Writing this inverse transform out longhand (i.e. using the formal definition, eqn. (2.8a)),

$$I(x) = \int \Phi_o(\frac{\sigma}{\lambda_n R}) \; [G(\sigma) \odot G^*(\sigma)] \; \exp[-2\pi i(\frac{\sigma}{\lambda_n R})x] d\sigma. \quad (2.19a)$$

Using the definition for the Fourier transform in this section (eqn. (2.23b)), and substituting eqn. (2.19a) into eqn. (2.30) gives

$$I_t(w) = [\int(\int\{ \Phi_o(\frac{\sigma}{\lambda_n R}) \; [G(\sigma) \odot G^*(\sigma)] \; \exp[-2\pi i(\frac{\sigma}{\lambda_n R})x] \; d\sigma)$$

$$\exp[2\pi ixw] \; dx)]^2 \cos^2(\pi wd). \quad (2.31)$$

Taking the transform of each side of eqn. (2.19) gives $\Phi_i(\frac{\sigma}{\lambda_n R}) = \Phi_o(\frac{\sigma}{\lambda_n R}) \; [G(\sigma) \odot G^*(\sigma)]$. This expression is substituted into eqn. (2.31). Then, repeating eqn. (2.22a) ($w = \frac{s}{\lambda_c L}$), collecting exponents, and rearranging the order

of integration in eqn. (2.31), the transform plane light intensity distribution is

$$I_t(\frac{s}{\lambda_c L})$$

$$= [\int \Phi_i \{\int \exp[-2\pi i x(\frac{\sigma}{\lambda_n R} - \frac{s}{\lambda_c L})]dx\}\, d\sigma]^2 \cos^2(\pi w d). \quad (2.32)$$

But, from the orthogonality properties of exponential functions (i.e. the transform of a constant is a delta function), the inner term is

$$\int \exp[-2\pi i x(\frac{\sigma}{\lambda_n R} - \frac{s}{\lambda_c L})]\, dx = \delta(\frac{\sigma}{\lambda_n R} - \frac{s}{\lambda_c L}). \quad (2.33)$$

Substituting eqn. (2.33) back into eqn. (2.32), and using the sifting properties of the delta function,

$$I_t(\frac{s}{\lambda_c L}) = [\int \Phi_i(\frac{\sigma}{\lambda_n R})\, \delta(\frac{\sigma}{\lambda_n R} - \frac{s}{\lambda_c L})\, d\sigma]^2 \cos^2(\pi w d)$$

$$= [\Phi_i(\frac{s}{\lambda_c L})]^2 \cos^2(\pi w d). \quad (2.34)$$

Note that,

$$\Phi_i(\frac{s}{\lambda_c L}) = \Phi_o(\frac{s}{\lambda_c L})\, [G(s) \odot G^*(s)]. \quad (2.35)$$

Substituting eqn. (2.35) back into eqn. (2.34), gives

$$I_t(\frac{s}{\lambda_c L}) = \{\Phi_o(\frac{s}{\lambda_c L}) \; [G(s) \otimes G^*(s)]\}^2 \cos^2(\frac{\pi s d}{\lambda_c L}). \quad (2.36)$$

In words, the halo intensity on the transform plane is the object plane frequency distribution times the autocorrelation of the pupil function. The halo itself is modulated by the 'cosine-squared' Young's fringe patterns.

Equation (2.36) can be characterized by considering two extremes. Consider the two limiting cases where the object contains many spatial frequencies (wide-band), or where the object contains relatively few spatial frequencies (narrow-band).

First consider the wide-band case. Recalling $I_o = FT\{\Phi_o\}$, if I_o contains many frequencies, then Φ_o will be nearly constant over a wide range, and will appear, in frequency space, as the rectangle function in Figure 2.6. (Here, it is assumed that the optical system is capable of imaging fine object structure; the case where system resolution is inadequate, that is, where object structure is very fine, is discussed in the section on sensitivity, below.) Thus from eqn. (2.36), and ignoring this constant, the diffraction pattern intensity will be given by

$$I_t(\frac{s}{\lambda_c L}) = [G(s) \odot G^*(s)]^2 \cos^2(\frac{\pi s d}{\lambda_c L}). \qquad (2.37)$$

which is simply the squared autocorrelation of the pupil function modulated by the cosine-squared term. Ignoring the last term, eqn. (2.37) is the halo intensity distribution for very fine object structure derived by Chiang [44], and Meynart [45], who each used the statistical optics approach.

If the imaging aperture is circular, the autocorrelation is given by eqn. (2.18a), thus eqn. (2.37) becomes

$$I_t(\frac{s}{\lambda_c L}) =$$

$$\{\cos^{-1}(\frac{s}{s_{max}}) - \frac{s}{s_{max}}[1 - (\frac{s}{s_{max}})^2]^{1/2}\}^2 \cos^2(\frac{\pi s d}{\lambda_c L}). \qquad (2.37a)$$

The autocorrelation of a circular pupil is shown in Figure 2.3b while the squared autocorrelation is plotted in Figure 2.7a, in transform plane coordinates. To review, Figure 2.3b is the frequency response (MTF) of the imaging lens while Figure 2.7a is the transform plane light intensity distribution. For a wide band of object spatial frequencies with moderate object displacement between exposures, the cosine-squared fringes are plotted in Figure 2.7b. (Tick marks on the horizontal axis are located at half-multiples of $\pm\pi$). The product of curves shown in Figures 2.7a and 2.7b represents eqn. (2.37a), and is plotted in Figure 2.7c.

(Figures are on following page)

Figure 2.7a Top - Squared autocorrelation of aperture function - light intensity distribution on transform plane

Figure 2.7b Middle - Cosine-squared (Young's) fringes for moderate object displacement between exposures

Figure 2.7c Bottom - Product of Figures 2.7a and 2.7b - transform plane intensity for fine object structure recorded through circular aperture for moderate object displacement

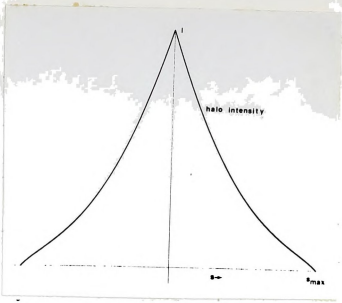

Figure 2.7a

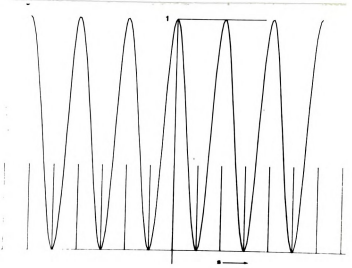

Figure 2.7b

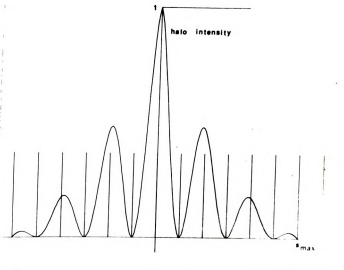

Figure 2.7c

Fig

Fig

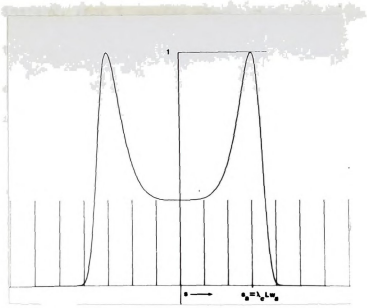

Figure 2.7d Narrow-band object spatial frequency distribution

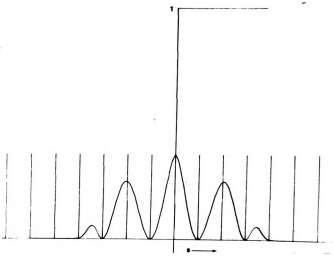

Figure 2.7e Product of 2.7a, b and d above - transform plane intensity for narrow-band object spatial frequencies recorded through circular aperture

Ass
acr
sha
val
fre
Fig
pro
and
2.7
int
fre
rec

V.

A.

Ser
spe
spe
dis
few
fri
ima
dis
sys

Assume instead, that I_o varies slowly with period ($\approx 1/w_a$) across the object surface. Φ_o will then exhibit a fairly sharp peak centered about the average spatial frequency value, $s_a = \lambda_c L w_a$. Thus, with narrow-band object spatial frequency content, the resulting Φ_o may be represented by Figure 2.7d, plotted in transform plane coordinates. The product of the functions represented by Figures 2.7d, 2.7a and 2.7b, according to eqn. (2.36), is plotted in Figure 2.7e. Thus Figure 2.7e gives the normalized transform plane intensity for a relatively narrow band of spatial frequencies appearing on the object surface, which have been recorded through a circular aperture.

V. SOME PRACTICAL ASPECTS

A. Sensitivity

Sensitivity of the speckle method depends on relative speckle size. If the specklegram consists of rather coarse speckle cells, or, looking at it another way, if film plane displacement is about the same size as the speckle cells, few fringes will appear in the diffraction halo, rendering fringe measurement difficult. If, on the other hand, the image has very fine structure (relative to the object displacement), sensitivity will be limited exclusively by system resolution. Each possibility is discussed below.

a. S

Sens
meth
smal
smal
case
as t
filt
frir
(2.2

Sub
rel
tha
int
fig
2.7
2.7
tha
two
int

a. Speckle shear approximately equal to speckle cell size

Sensitivity of an interferometric displacement measuring method is a function of the recorded speckle size. The smallest detectable displacement is fixed by the size of the smallest individual speckle (shadow) cells. Consider the case where the smallest speckle cell is about the same size as the speckle shear, that is, when $1/w_{max} \approx d$. Upon filtering such a specklegram, the distance between adjacent fringes is given by eqn. (1.1) as $S = \lambda L/d$. From eqn. (2.26b), the maximum halo radius is found to be

$$s_{max} = 2w_{max}\lambda L.$$

Substituting eqn. (1.1) into eqn. (2.22a), and using the relationship between speckle size and shear, it is seen that, $s_{max} = 2S$. The resulting diffraction halo light intensity distribution is illustrated in Figure 2.8a. This figure, according to eqn. (2.37a), is a product of curves 2.7a and 2.7b, where the cosine-squared extrema in Figure 2.7b have simply become more coarse (moved outward). Note that there will appear but two distinct minima; the outer two will likely be obscured by rapidly diminishing halo intensity.

Fig

Fig

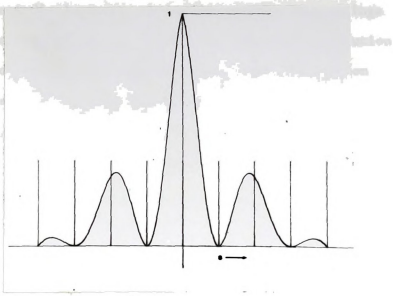

Figure 2.8a Transform plane fringes for object displacement which is of the same order as speckle size

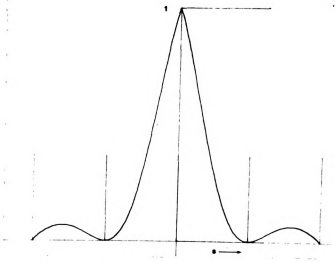

Figure 2.8b Transform plane fringes for object displacement which is less than speckle cell size

As object displacement, d, becomes smaller yet, fringe extrema move farther outward. The practical resolution limit of the white-light technique, then, depends on system noise and on the actual shape of the halo intensity envelope. A reasonable guess as to when the fringe minima can no longer be distinguished would be at $1/2w_{max} \approx d$. Following the same reasoning as above, this is where

$$s_{max} = S.$$

The transform plane light intensity distribution for this limiting situation is shown in Figure 2.8b. Object displacement smaller than 1/2 of the speckle cell size would certainly obscure extrema location, reducing confidence in primary data.

b. Speckle shear much greater than speckle cell size

If the object structure is very fine, recorded speckle size is governed by either aperture size or system resolution. Aperture size controls the spatial frequency appearing in the image as explained in the imaging section above. Clearly, only those cells which are larger than a certain minimum will be imaged. Thus, for a given system, the recorded speckle size is inversely proportional to the F-number (= F# = focal length/aperture diameter). Chiang [6]

has demonstrated this effect showing smaller halo diameters corresponding to increased imaging F# with all other conditions equal.

Resolution, that is, the ability to resolve two nearby points, is theoretically a function of F# as prescribed by eqn. (2.18b). At the glacier imaging F#'s, (8 and 16) for example, the maximum object spatial frequency admitted by the imaging lens was

$$u_{max} = \frac{2a}{\lambda R} = \frac{1}{\lambda F\#} = \frac{1}{6x10E\text{-}4x8} \approx 208 \text{ lines/mm},$$

$$\text{and, } \frac{1}{6x10E\text{-}4x16} \approx 104 \text{ lines/mm},$$

for the year-one and -two camera systems respectively. It will be seen in the next chapter that the practical resolution limit is, of course, less than these values. In a real imaging system, therefore, resolution is not dependent solely upon aperture size as given by eqn. (2.18b). There is further 'spreading' of an object point into an image patch as energy is diffracted traversing through the system.

Resolution is quantitatively evaluated in terms of the point spread function (PSF), alluded to above. The Fraunhoffer (far-field) diffraction pattern of a point source, imaged

through an aberration-free circular pupil, is shown by Born and Wolf [20] to be the familiar Airy disk. Airy disk intensity is a decreasing Bessel function. Thus, image plane intensity is given by

$$I(s') = \left(\frac{2J_1(v)}{v}\right)^2, \qquad (2.38)$$

where $v = \frac{2\pi a}{\lambda R} s' = \frac{\pi}{\lambda F\#} s'$. s' is the radial distance from the center of the pattern, a is the radius of the pupil, R is the focal length of the imaging lens, λ is the illuminating wavelength and J_1 is the Bessel function. After Welford [37], this normalized intensity distribution is plotted in Figure 2.9. If two object point sources are sufficiently close, their respective Airy patterns will add and, at some minimum separation distance, their images will become indistinguishable. Lord Rayleigh, in 1879, proposed that two nearby points of equal intensity, are just resolvable if the principal intensity maximum of one coincides with the first intensity minimum of the other. The Bessel function zero (i.e. the first dark ring of the Airy disk) occurs when $v \approx 3.83$. According to Rayleigh's criteria, the minimum resolvable distance between object points (with unit magnification) is therefore

$$s'_{min} \approx \frac{\lambda F\#}{\pi} 3.83 \approx .61\lambda F\#. \qquad (2.39)$$

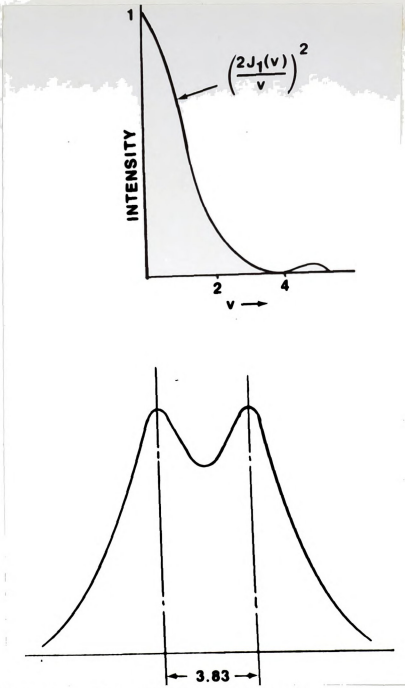

Figure 2.9 Top - Airy disk intensity distribution - point spread function for circular aperture

Figure 2.10 Bottom - Rayleigh criterion for minimum resolvable separation between object points (referred to film plane)

The additive intensity of two spectral components which are just resolved are shown in Figure 2.10.

Note that the Airy pattern is simply the result of diffraction. It is the PSF of a substantially perfect system. In the presence of aberrations the PSF changes shape in a complicated way and may deviate to a multi-peaked curve as shown, for example, in Figure 2.11. Quantitative effects of specific or combinations of aberrations on PSF are not readily found. In fact, such tests are difficult to perform on specific instruments. Welford [37], however, generalizes that minor aberrations lower the central intensity, and more light appears in the dark rings, while the half-width of the central maximum does not change. Thus, with increasing aberrations, the image of a point source simply appears as a larger, less well-defined patch, reducing resolution.

Maximum film plane displacement sensitivity, on the other hand, is exceeded when speckle correlation is lost, that is, when fringe patterns are no longer discernible in the filtering process. For coherent imaging, Archbold and Ennos [8] have taken this value to be about 5-10 speckle diameters. Cloud's experiments [5], using different optics, confirm this estimate. Corresponding sensitivity estimates for the white light case, however, are not found in the literature. Upon filtering, white-light generated speckle

Fi

Fi

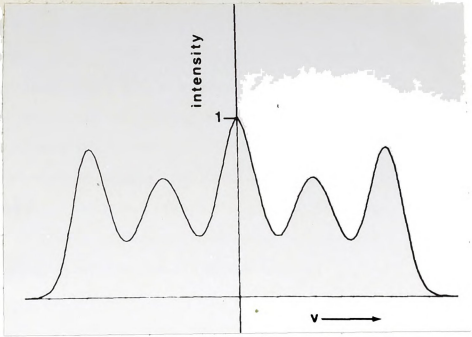

Figure 2.11 Typical non-ideal point spread function for which the Rayleigh criterion will be invalid

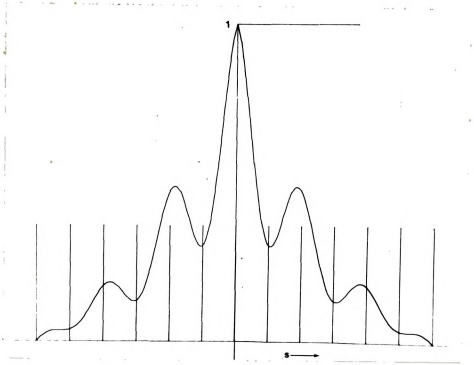

Figure 2.12 Fringe pattern shift with non-unity visibility for moderate object displacement

patterns produce greater optical 'noise' than the coherent counterpart. This is due, in effect, to less contrasty 'pinhole' edges of the diffracting speckle cells. It is expected that the maximum range of displacement sensitivity (referred to the average speckle diameter) is less then that for coherent imaging. Rigorous experiments on the upper bound are not often reported since, in this range, other displacement measuring methods such as moire and photogrammetry are more commonly used.

B. Fringe pattern measurement

The envelope which modulates Young's fringes (shown in Figure 2.7a) shifts maxima toward the center of the interrogating beam. This effect is seen in Figure 2.7c, where the actual maxima, for example, are located at the tick marks $\pm\pi/2$, but the apparent maxima are somewhat closer to the origin. Therefore, it is better to compute displacements from minima, but, as Kauffman [51] shows, this will only be exact when such minima have zero intensity.

In practice, fringe patterns will be superimposed with 'dc' noise resulting in a typical transform plane intensity distribution shown in Figure 2.12. This figure was generated using the (apparently empirical) formula given by Kaufmann [51] which accounts for such dc offset:

$$I_v(\frac{s}{\lambda_c L}) = \{\cos^{-1}(\frac{s}{s_{max}}) - [\frac{s}{s_{max}}](1 - [\frac{s}{s_{max}}]^2)^{1/2}\}^2$$

$$[\frac{1-v}{1+v} + \frac{2v}{1+v}\cos^2(\frac{sd\pi}{\lambda_c L})]. \quad (2.40)$$

Here

$$v = (I_{max} - I_{min})/(I_{max} + I_{min}), \quad (2.41)$$

is Michelson's formula for fringe visibility, and I_{max} and I_{min} are the maximum and minimum intensity values of the cosine squared fringes. Note that eqn. (2.40) is simply eqn. (2.37a) with visibility incorporated into the second factor.

The parameters used to generate Figure 2.12 are the same as those used for Figure 2.7c (except for visibility), thus allowing comparison. For a typical fringe visibility factor of 0.4, Figure 2.12 shows a slight shift of fringe minima away from the origin. Kauffman [51] has shown that such a fringe shift is dependent upon recorded spatial frequency; lower frequencies result in higher errors. For the present study, Kauffman's analysis predicts 10 to 15% error for measurement based on fringe minima. Unless the diffraction halo is removed prior to determination of fringe spacing, it is more accurate therefore, to calculate displacements from minima.

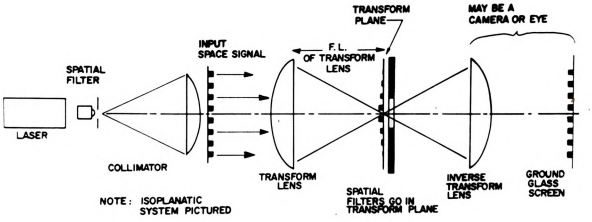

Figure 2.13 Whole-field filtering scheme

C. Other limitations

Problems associated with practical application of the white light speckle technique have been described by many authors. Archbold et al [4] note that object surface tilt, out of the plane of the film, can result in defocus. The tilt problem is aggravated by large ratios of focal length to object distance where the subject is close to the camera and the depth-of-field limitations of the imaging system is exceeded. Chiang [7] writes that surface tilt can also result in apparent ficticious in-plane displacement. With large extended objects located far from the camera, the tilt problem is considered inconsequential.

V. WHOLE-FIELD FILTERING

Optical Fourier processing (c.f. [9], [10]), is well suited to delineating components of homogeneous spatial frequency recorded on photographic transparencies. Figure 2.13, reproduced from Cloud [64], depicts a specklegram placed in the input plane of such an optical filtering system. An advantage is that sensitivity can be varied after the data are recorded. Such a feature is especially valuable in experimental work where strain magnitudes are not known beforehand. If the displacement across the image field is not homogeneous, however, whole-field fringes can be viewed by placing an aperture in the transform plane. Fringes thus

a

c

a

e

p

w

p

l

V

R

T

d

a

f

appearing superimposed on the image, represent displacement contours in the direction of the aperture from the optical axis. Froely et al [20], Asundi and Chiang [6] and other experimenters, have suggested, however, that the point-by-point method yields higher fringe visibility and accuracy where object surface displacement, referred to the film plane, is not uniform. Experimental verification of these limitations are explored in Chapter 3.

VI. SUMMARY

Recording and analysis of optical data have been outlined. The result is a remarkably simple method to sense small displacements of remote objects. Straight forward application of this method to a non-laboratory object is found in the next chapter.

CHAPTER 3

METHOD AND RESULTS

I. FIRST YEAR EXPERIMENTS

A. Preliminary development tests

Choice of photographic equipment for the first year study was dictated by availability and portability. A Linhoff view camera and Schneider-Kreuznach Xenar coated lenses with focal lengths 500mm, 360mm and 300mm were selected. Quality optics and rugged construction combined with a variety of accessories made this instrument a good choice in the event of potentially adverse and otherwise unknown field conditions.

Use of the 4x5 format is common in experimental mechanics practice. This format is available in film and glass plate coated with a variety of scientific emulsions. Laboratories, including those at Michigan State University, are geared to processing and handling these films; the 4x5 was the format of choice.

Initial photography experiments utilized large objects under natural illumination. All were found near the Engineering Building and all were imaged on several different emulsions

in both film and plate. Experiments were conducted in order to establish the necessary mix of F#, focusing technique, exposure time, processing method, and other variables which would give contrast and resolution required for fringe generation.

The Communication Arts Building, located about 250m south of the experimental mechanics laboratory window, was the first object photographed, Figure 3.1. Recently constructed of red brick and illuminated by an early evening sun, the north face appeared to afford the necessary contrast. Trained on the center of the ground glass placed in the image plane, a 60x microscope was used to magnify and focus the image.

It was noted that, under magnification, outdoor images 'wiggled' perceptibly during this, and subsequent experiments. It was difficult to ascertain whether such quiver was caused principally by camera motion or by refraction gradients of the turbulent media through which the images were shot. High summer afternoon ambient temperatures seemed, however, to exacerbate the problem.

After careful focus, Kodak SO-253 High Speed Holographic film was exposed for 1/15s at F#8, using a 360mm lens. Film specifications, developing solutions and other processing details can be found in Appendix I.

Figure 3.1 Communication Arts Building - artificial field displacement experiment subject

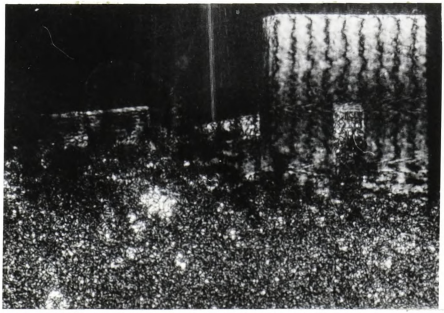

Figure 3.2 Whole-field fringes from Communication Arts Building image

Pointwise filtering (as shown in Figure 1.3) of the processed image produced a diffraction halo about 34mm in diameter. Other parameters of the filtering exercise were: filtering (interrogating) beam wavelength, λ = 6.3x10E-4mm, and filtering (transform) distance, L = 1000mm.

Recall from the previous chapter that the maximum spatial frequency content of the specklegram is given by the size of the diffraction halo. Assuming Burch and Tokarski's [3] ideal rectangular diffuser, the maximum halo radius is $2w_{max}$ diffraction units as seen in Figure 2.7a. According to eqn. (2.26b),

$$2w_{max} = s_{max}/\lambda L = \frac{17mm}{(6.3x10E\text{-}4\ mm/cycle)(1000mm)}.$$

Thus

$$w_{max} \approx 13.5 \text{ cycles (or lines)/mm}.$$

Several fringe orders were apparent within the halo. Based on the fringe minima separation of 5.2mm, accounting for 'fringe shifting' equal to roughly 10% and using eqn. (1.1), the pitch of the specklegram 'grating' was

$$6.3x10E\text{-}4x1000/5.2 \approx .12mm.$$

This value agrees well with the measured pitch of the brickwork, calculated as follows. Each course of red brick

rises roughly 9cm. Based on this pitch, specklegram spatial frequency is

$$\frac{1 \text{ cycle}}{90\text{mm}} \times \text{demagnification.}$$

Taking

demagnification = object distance/image distance

where the lens law dictates that image distance ≈ focal length for remote objects. Specklegram spatial frequency is then

$$\frac{1}{90} \times \frac{250}{0.36} \approx 8 \text{ lines/mm or } 1/8 \approx 0.13\text{mm/line.}$$

Henceforth, fringe spacings were taken from minima and corrected for shifting.

A double exposure of the Communication Arts Bldg., with the camera back rotated about its normal approximately 20min. of arc between exposures, resulted in very small, but nearly uniform, displacement of the image in the horizontal direction. Such motion resulted from the position of the building image on the film with respect to the center of rotation of the camera back. The building facade appeared at the 12 o'clock position and near the edge of the film.

Thus, very small rotations of the camera back appeared as nearly homogeneous building image displacement. Pointwise filtering did not yield Young's fringes indicative of such displacement. This was not surprising since microscopic examination of the specklegram showed that horizontal spatial frequency components (i.e. vertical lines of mortar) exhibit much less contrast than vertical components. Whole-field Fourier processing, however, resulted in good visibility of fringe patterns indicating horizontal image shear, up to order 2, as shown in Figure 3.2. It was evident that uniform displacement is more easily discerned using the whole-field method. Suitability of the whole-field method, in the case of non-uniform displacements, was determined in subsequent experiments.

The asphalt surface of a partially shaded walkway lying about 10m beneath a third floor laboratory window served as the next subject. Young's fringes, Figure 3.3, appeared when the artificial field displacement experiment described above was repeated using the same film (500mm lens, F#8, 1/30s each exposure). Pointwise filtering did not produce fringe patterns at every point on the image because of depth of field limitations; nevertheless, this experiment indicated that the camera/film system was capable of producing the desired image structure without direct sunlight illumination.

The final development subject was a partially graveled parking lot located west of the Engineering Building, Figure 3.4. Random patterns such as tire tracks and grading lines found here proved to be a good photographic approximation to a glacier surface. Artificial field displacement experiments were repeated with an evening sun angle of approximately 60 degrees from the zenith. Photographed from a perch atop the Engineering Bldg., about 15m high, the surface extended from 100 to 200m distant. A point about 150m from the camera site was precisely imaged near the center of the ground glass via microscope. Depth-of-field was adequate as the image later proved to be focused from top to bottom of the plate. It became standard practice to focus on points lying near the top-to-bottom middle of the field. Final film processing resulted in rows of classic speckle pairs which, when scanned pointwise from the center outward, produced increasingly fine, rotating Young's fringes. This behavior was exactly as expected. Fringes generated from image points which lie near the center of rotation suffer relatively small displacement; according to eqn. (1.1), fringes were correspondingly coarse here. The fringe bands became finer as the radial distance from plate center increased. The two parking lot images, slightly rotated with respect to one another, resulted in a series of Young's fringes whose axes were perpendicular to the local displacement vector. As the image was scanned along a chord, the relative angle of displacement changed. This was

Figure 3.3 Fringe bands (extending from upper left to lower right) enclosed in halo - from artificial field displacement tests - subject, asphalt walkway

Figure 3.4 Gravelled parking lot image

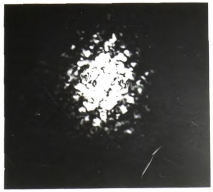

Figure 3.5 Diffraction halo and fringes (extending from lower left to upper right)-subject, parking lot

indicated by rotating fringe axes. Figure 3.5 is representative of the fringe patterns produced across the central portion of the image.

Performing a calculation similar to that above, the maximum spatial frequency of the parking lot image was inferred from the size of the diffraction halo during pointwise filtering. The spatial frequencies of the images were about 18.3 lines/mm @ F#22 and 25.4 lines/mm @ F#11, (using Kodak High Speed Holographic type SO-253 film). The higher spatial frequency content of this image (compared to that of the brick facade of the Communication Arts Bldg.) was attributed to the oblique viewing angle as well as to the fine structure of the coarse sand and pea-graveled surface.

In contrast to the results of the pointwise method, whole-field, Fourier optical processing of the same parking lot specklegram yielded fringes of near zero visibility. In this whole-field process, it was noted that fringe visibility was directly related to the uniformity of the spatial frequency of the input signal. It was also noted that ice displacement is not, in general, uniform across the large areas of glacier surface which would be recorded in one frame. In the event of nonhomogeneous field displacement, pointwise filtering, as in Young's experiment, "is more tedious than the whole-field approach...[but] displacements thus obtained are more accurate and fringe

quality is much better", Asundi [6]. Henceforth, study was devoted to the creation of photographic images having sufficient diffraction efficiency to produce quality Young's fringes.

Artificial field displacement experiments were repeated using glass photoplates. Focusing was somewhat more reliable using plates in place of film. Misfocus, resulting from both film warping and imprecise adjustment, was reduced using Kodak High-Speed Holographic type 131-02 glass plates and an additional refinement in technique. A rough image was focused in the normal view camera manner on ground glass, the glass having the same dimensions and index of refraction as the photographic plate. A microscope, mounted on the camera back, was focused on the ground glass at a point near the center of the image. The microscope was thereby positioned in proper relation to where the emulsion plane would be located during actual photography. The ground glass was then carefully removed from the camera, leaving the microscope focused near the image plane. While viewing through the microscope, the image was then refocused on the image plane by adjusting the camera back/microscope assembly. This technique is sensitive because the depth of field of the microscope is very small. The error which was introduced by focusing initially through the ground glass, amounted to less than 0.3mm. For the purposes of the present work, this level of defocus was negligible. This

conclusion is based on Figure 2.4, where the camera system frequency response (for defocus equal to 0.3mm) lies between the curves marked 0 and 1. Microscope focusing became standard practice.

Experiments to estimate the practical resolution limit of the lenses were performed using a standard optical bar chart and a sensitive microscope trained on the image plane. Bar charts contain arrays of lines spaced at uniformly increasing spatial frequency. After positioning the chart in an Engineering Building hallway at an appropriate distance from the camera (58m, in this case), a point near the image center was magnfied through a microscope and the pitch at which the lines become indistinguishable was estimated. This value was taken as the practical resolution limit of the imaging lens. At F#8 and, at this object distance, the maximum distinguishable spatial frequency of the imaging lens was about 1.1 lines/mm (28 lines/in) at the object; at F#11 the value was about 0.94 lines/mm (24 lines/in).

Final experiments in preparation for glacier field work included a crude attempt at aperture filtering. An opaque circular disk was cut from black electrical tape and placed at the center of the 500mm lens. Such a mask, sized about one-fourth of the lens aperture, acts as a high pass filter. With this mask in place, standard artificial field

displacement tests, processing and pointwise interrogation, resulted in reduced fringe quality. Evidently, lower spatial frequencies than those admitted by the filter were required for good fringe quality and energy content in the range of frequencies eliminated by a yet smaller disk was small enough to have negligible effect. It was concluded that images having good diffraction efficiency are formed from low-frequency components. Aperture filtering experiments were discontinued.

Two other photographic emulsions were also tested. Kodak Minicard SO-424 Scientific Film was used in the parking lot tests with marginal results. The visibility of fringe patterns thus produced were decidedly less than those produced by the holographic film. Tests with Kodak SO-649F Spectroscopic plate produced moderately visible fringes, but this emulsion proved to be relatively slow in white light. Exposure time just over one second exceeded the timer range on the available shutters, possibly necessitating manual shutter operation. With the field season impending, efforts were concentrated on developing a dependable field technique using glass plate, while testing other media when the opportunity arose.

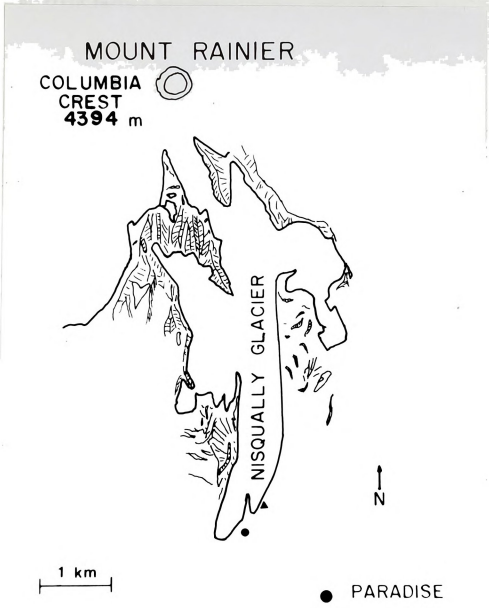

Figure 3.6 Nisqually area map - the symbols ● and ▲ indicate the year-two camera locations

B. Field tests - Nisqually Glacier, Washington

Artificial field displacement experiments were repeated at the Nisqually Glacier, Mt. Rainier National Park, WA, USA, Figure 3.6. Changes in lighting, subject size, camera positioning and other factors made recalibration necessary. After several days of trial, cursory examination indicated fringe patterns approaching the quality of those produced during the initial tests were generated. Images recorded from several perspectives, all within 1km of the glacier snout, were successful. A small (low) sun angle on the south-flowing glacier surface surface yielded the best fringe quality; hence, it was decided to initiate time-interval, double exposure experiments during morning.

With a diffraction halo radius measuring roughly 10mm, the maximum spatial frequency of the specklegrams recorded during glacier-site artificial displacement tests was about 7.9 lines/mm.

Site accessibility compromised camera location. A site located too far from the equipment vehicle would require a pre-dawn hike up unfamiliar terrain; locating the camera too close to public parking would tempt curious, if well-meaning, tourists. Fearing damage to fragile one-inch-thick topsoil, Park Service personnel did not allow camping near potential camera sites; equipment remained unattended for

overnight periods. The camera was eventually located on the side of a hill, partially hidden by a clump af trees, about 50m up from a relatively seldom traveled path.

The Nisqually icefall constitutes the steepest portion of the glacier surface. Theory predicted relatively rapid ice flow rates in this area. It was decided that the icefall offered the best possibility from which to record discernable ice displacements during convenient time intervals. As explained in Chapter 2, sensitivity of the interferometric method is fixed by the spatial frequency of the image: smaller speckle cells result in higher sensitivity. Based on earlier glacier-site artificial displacement experiments, the smallest resolvable ice displacement was $1/7.9 \approx 0.13$mm, referred to the film plane. Accounting for magnification and perspective, the estimated icefall velocities of very roughly 1 meter/day would render speckle shear within the discernable range.

Image speckle pattern is a function of both surface roughness and illumination position. A 24 hour time-exposure interval resulted in nearly identical sun angles thereby increasing precision. Thus, the image was centered near the base of the icefall and a twenty-four hour time-lapse interval was chosen as the starting point for field experiments.

With favorable weather, two twenty-four hour, double exposure experiments were conducted at, or near, the hillside site. High Speed Holographic emulsion, 500mm lens, F#8, 1/8s each exposure was used, with the camera mounted on a sturdy, commercially available tripod. Both the film, in the first trial, and the photoplate in the second trial, suffered from excess camera motion incurred between (or during) exposures. Excessive motion appeared in the image as rigid body displacement and may be attended by loss of speckle correlation. A double exposure having virtually zero time interval was recorded to determine, qualitatively, camera motion caused by shutter operation. Microscopic examination of the resulting short-duration image did not reveal rigid body displacement. The conclusion was that tourists, animals (many of which appeared to be very tame), weather, natural settling of the tripod mount or perhaps seismic activity related to nearby, bestirred Mt. St. Helens could have caused the shift during the 24 hour interval. A site which assured sturdy, undisturbed camera support was required.

The glacier surface proved to be bright enough to image on the relatively slow Spectroscopic emulsion. Contrary to expectations, the shutter timing mechanism, supplied with the camera had sufficient range to accomodate this photographic medium. Thus, some time-lapse experiments were performed using this plate.

Interposing the artificial displacement tests and double exposure tests were serial, single exposures recorded on a daily basis. In these experiments, the image was recorded alternately on forward and reverse emulsion. Such an arrangement allows the processed photoplates to be superimposed upon one-another as right and left hand images. In this manner, and after the manner of Adams [32], the intent was to place fixed objects, such as rock outcrops appearing in the image, in exact registration, thereby subtracting rigid body motion. Three degrees of freedom complicated plate positioning. Efforts were subsequently concentrated on developing the double exposure procedure.

With intent to isolate the motion problem, double exposure photography was conducted at other sites. Images having time intervals of four and twenty-four hours did not yield Young's fringes but indicated an important cause of camera movement. A four-hour double-exposure, using High Speed Holographic film, 500mm lens, F#22, 1/50s each exposure, showed no ice or rigid body displacement. An interval of fourty-eight hours, on the other hand, resulted in complete loss of speckle correlation owing to excessive camera motion. Yet longer time intervals exacerbated the motion problem, suggesting that gradual settling of the tripod over time was a major contributor. Earthen settling rates tend to decrease over time. The conclusion was that long-term sites would tend to offer increased camera stability; a

carefully selected camera site was to remain unmoved during subsequent field work.

Various means of supporting the camera were not effective until, finally, the instrument was mounted on a large rock. Figure 3.7 was reproduced from the resulting twenty-four hour, double exposed photoplate (Spectroscopic 649-F plate, 500mm lens, F#8, 1s each exposure). Upon interrogation, rows of speckle pairs produced Young's fringes across much of the glacier surface image. Two such fringe patterns appear in Figure 3.8 and Figure 3.9, recorded with the original transparency unmoved. Figure 3.8 was produced as a narrow laser beam was diffracted by a portion of icefall image while Figure 3.9 was similarly produced from a point at a lower elevation, about mid-glacier. The slight rotation of fringe axes was expected, attributed to a change in perspective. Appearance of Young's fringe patterns, indicative of ice displacement, demonstrated data gathering practicability of the white light technique and culminated the 1981 field season.

C. Fringe pattern analysis

The maximum spatial frequency of the glacier specklegram, corresponding to the 10.5mm diffraction halo radius, was about 8.3 cycles/mm. Typical speckle cells, viewed under the microscope and measured with a finely graduated scale,

Figure 3.7 Print of double-exposure 24hr plate - Nisqually

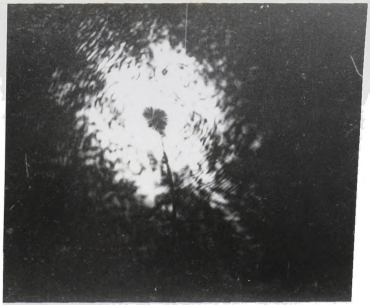

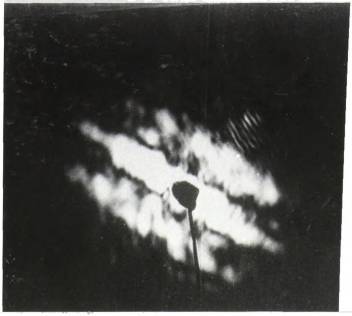

Figure 3.8 Top - Fringe bands from Nisqually Icefall

Figure 3.9 Bottom - Fringe patterns from Nisqually down-glacier (bands extend from upper left to lower right)

exhibited roughly the same size (i.e. 1/8.3 ≈ .12mm). Note that the intensity of these fringe patterns roughly correspond to the intensity distribution plotted in Figure 2.8a for which speckle cell size and shear were assumed equal. It was possible to obtain useful fringe axis separation and orientation measurements as described below.

Young's fringe patterns, gleaned from the double exposed glacier surface image, were transformed into ice displacement rates in order to compare the data with information gathered by conventional methods. Comparison was made to determine technique deficiencies and prepare a list of recommendations to be implemented during subsequent study.

Data analysis, that is transformation of fringe pattern parameters into surface velocity maps, required assumptions regarding optical magnification, camera motion and perspective. The process evolved into the steps enumerated below:

(1) Young's fringes were logged from several points of the double exposed, twenty-four hour image. Fringe separation and angle of the fringe axis with respect to vertical were measured. Trees visible in the image foreground of Figure 3.7 served as vertical reference. The position of image points relative to prominent features such

as rock cleavers, cirques, and silhouettes appearing on both the image and topological map were noted. In this manner the glacier surface topological map location corresponding to the particular image point was determine fairly accurately (within about 40m). At each map location, the slope (i.e. surface normal) was then approximated using map contour lines. Nine points, resulting in the best 'spread' across the glacier surface, were selected. Employing eqn. (1.1), a gross displacement vector was calculated at each point, in image plane coordinates.

(2) Microscopic examination of the double exposed image revealed displacement of a fixed object; in this case, a large boulder resting on a bare rock surface. The rigid body displacement vector of this point, again determined in image plane coordinates, was measured with a finely graduated scale and protractor.

(3) Assuming uniform image plane camera motion, a specially written computer routine vectorially subtracted rigid body displacement from the gross displacement found in step (1), the algorithm again operating in image plane coordinates. The difference is net ice displacement in image plane coordinates.

(4) Net ice displacement was projected onto the glacier using surface normals found in step (1) and the

magnification, defined earlier. Figure 3.10 depicts the computer projection algorithm.

Nisqually Glacier ice displacement for selected surface points over a twenty-four hour period in late August, 1981, Figure 3.11, resulted. Two additional assumptions were required in order to arrive at this particular ice velocity map. First, since interferometry does not reveal a sign, it was assumed that ice flows (generally) downhill. The second assumption, that of correct rigid body displacement direction, was less clear intuitively. Another displacement map could be generated, for example, using the same data but assuming the opposite displacement direction. Figure 3.11 is simply the most reasonable since the alternative computation gave ice displacements of two to three times greater magnitude.

The ice displacement magnitudes, extracted by the white light technique, corresponds to those reported by Hodge [28], who used conventional methods. The earlier research team was prevented by severe weather, Hodge writes, from studying flow in the higher elevations. In areas for which comparisons can be made (roughly points 7 and 8 in Figure 3.11), Hodge's two year study gives centerline flow rates of 0.4 meters/day while the white light technique yields 0.6 meters/day.

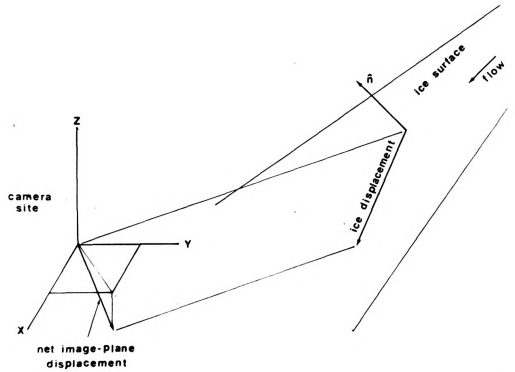

Figure 3.10 Computer projection algorithm

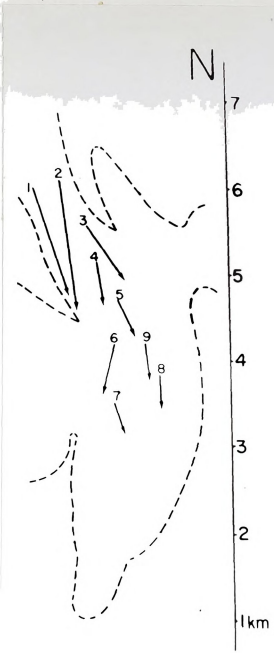

Figure 3.11 Final results from year-one

D. Year-one preliminary conclusions

These encouraging results lead to the conclusion that the white light technique was feasible in application to glacier study. Preliminary conclusions, based on first year results, especially those affecting development activity the following field season, are enumerated below:

(1) Double exposed images were more practicable than single, serial exposures because of the difficulty in superimposing images in perfect registration.

(2) Surveying methods to locate features found on the photographic image were needed. Location of many significant features would increase the precision with which fringe generating image points were located on topological maps. Also, to increase precision, a vertical reference indicator should be included in the photographic image.

(3) Being of the same order of magnitude as net ice displacement, apparent image plane rigid body displacement was a major factor affecting precision. Three steps were suggested as partial remedies:

(a) Apparent movement suffered by all image points was to be reduced with the use of sturdier camera mounting.

(b) Camera motion, however small, is likely during time-lapse photography. Quantification of this residual motion is discussed below.

Displacement in a plane (in this case, the apparent motion of 'fixed' objects in the film plane) can be resolved into two components, translation and rotation. Referring to Figure 3.12, planar motion of any given point, say point M, can be thought of as a simple translation parallel to some reference point translation, P to P', followed by a finite rotation about that same reference point, P'. The rotation, through a so-called Euler angle (angle θ), suffered by any line in the plane is the same rotation suffered by any other line. The difference in the motion of any two points is accounted for by the difference in their respective position vectors relative to the translated reference point. In the diagram, relative position vectors are designated R_z, where the variable z is the label of the point whose rigid body displacement is to be determined. Three pieces of displacement information about two points in this plane are needed to completely specify translation and Euler angle parameters. They are the two components of the rigid body displacement vector of one 'fixed' reference point appearing in the double exposed specklegram, point P, and the direction cosine ($\cos\phi$) of the displacement vector of reference point Q. Coordinates of other points relative to

reference point P is sufficient, then, to delineate rigid body displacement of all points lying in the image plane. It was decided that two reference points, such as P and Q in Figure 3.12, be incorporated into the image during the second field season.

(c) As a final check of the rigid body displacement vector estimates (performed in step (2) of the prior section), it was proposed that two independent data sets be acquired simultaneously using a stereo camera system. Separate ice velocity maps, constructed as described above, were to be compared, establishing confidence levels.

(4) Figure 3.11 shows displacement rates of points widely scattered about the glacier surface. Greater detail, perhaps revealing icefall margin shear rates, would be realized by either photographing from a closer vantage point or using telephoto lenses. A perch close to the most active part of the surface was not accessible to the field crew on a daily basis; use of long focal length lenses was the alternative.

(5) Assuming decreasing earth settling rates, camera stability should increase with site installation time. During subsequent field work, camera locations would remain fixed for the duration of the field work stay.

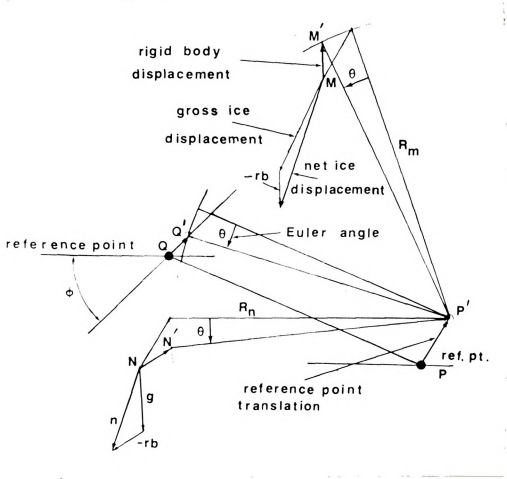

Figure 3.12 Euler angle algorithm

II. YEAR-TWO EXPERIMENTS

A. Preliminary development tests

Technique development centered on implementing year-one conclusions. Equipment was assembled and methods were tested in a manner similar to that of the previous season. Details of initial development tests are not repeated in this section unless differences between this and the previous work were significant.

Alterations in the program were primarily accountable to camera hardware changes. Identical cameras were assembled from military surplus 916mm, F#5.6-16, uncoated aerial photography lenses and rotating plate holders. Lenses and telescoping camera backs were mounted on either end of a short length of 6in., Schedule 80 PVC tubing, Figure 3.13. Camera-back mounted microscopes (again, 60x) were used to precisely adjust focusing micrometer screws. Machinists levels, also mounted on the camera backs, were used to orient the photoplate into the 'vertical' position.

In their original form the military surplus lenses were not suitable for the intended purpose. Very stiff springs powered the internal shutters; triggering the shutter visibly jarred the camera. Experiments showed the timing mechanism was not repeatable in any range; the exposure

interval being very roughly dependent on the extent of spring windup. After the shutters were modified to operate manually with remote cable release, however, exposure intervals in ranges over one second proved repeatable. Exposure times in this range necessitated the use of the relatively slow Kodak 649-F Spectroscopic emulsion.

Initial photography experiments were, once again, carried out using the gravel parking lot west of the Engineering Bldg. Artificial field displacement tests were repeated with similar results: Young's fringe patterns, though noisy, were produced from the gravel surface image (using Spectroscopic 649-F plate, F#16, 2s each exposure).

The very broad spectral sensitivity of Kodak 649-F Spectroscopic emulsion diminished fringe quality by imaging chromatically aberrant frequencies. The effect known as dispersion converges different colors at different focusing distances. Focusing on one color defocuses other wavelengths. The unfocused energy remains in the optical system and serves to diminish the image contrast which is necessary for good diffraction efficiency. Such a reduction is manifested in the filtering process by diminished halo size. Therefore, lens modifications, narrowing input spatial frequency content (band pass filters) or limiting the radiation wavelength to the image, were tested. It was found that colored cellophane lens filters or spatial

frequency masks (as in year-one) necessitated long exposure times with no appreciable gain in fringe quality. Refraction gradients in air resulting from atmospheric turbulence, random low level oscillations of the earth and other 'background noise', either mechanical or electromagnetic in nature, reduce the sharpness of any photographic image. Long exposure times, necessitated by the use of colored filters or masks, exacerbate these problems. Thus, lens modification experiments were abandoned. Focusing in the middle of the range between the 'sharp blue' and 'sharp red' positions was the compromise.

Resolution tests as described in section A of this chapter, were conducted with the year-two equipment and with the target optical bar chart placed at 130m from the camera, again in an indoor hallway. At the aperture setting used for all of the year-two experiments, F#16, it was possible to distinguish lines having spatial frequency up to about 0.51 lines/mm (13 lines/in)at the object.

After perfecting focusing technique using Spectroscopic film, artificial field displacement tests imaged a relatively broad frequency spectrum of about 19.8 lines/mm, inferred from the diffraction halo size, using eqn. (2.26b).

Kodak Minicard SO-423 film, being relatively slow in white light, seemed to be suitable for use in the manually

operated shutter cameras. Several single and double exposure experiments resulted in apparent misfocus. This indicated that either the emulsion had inadequate resolving power to image the necessary structure or film warping was causing misfocus. Field work was to be conducted using Spectroscopic plate.

Feasibility study funding was earmarked for application of the white light technique to two separate glaciers. The Nisqually glacier was chosen as the first to be photographed with the newly assembled, specialized equipment for several reasons. An existing body of knowledge regarding ice flow behavior was available for comparison purposes, the site is accessible, the climate relatively benign (in late August) and the field team was familiar with the area. Workers were to perfect data acquisition methods at the Nisqually and then travel to the Ptarmigan glacier, near Juneau, Alaska. The mile-high icefield abutting the Alaskan coast was to provide a more rigorous testing ground. Unexpectedly well studied, the Ptarmigan exists in a severe, changeable and remote environment.

Satisfied with initial test results and armed with 13 boxes of equipment, tools, supplies and luggage, the expedition set out first for Mt. Rainier National Park, WA.

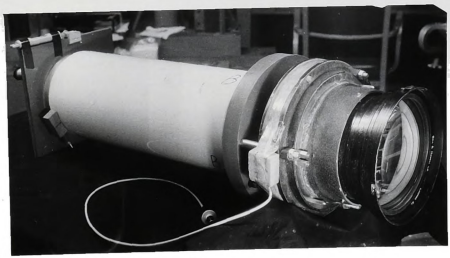

Figure 3.13 Specialized camera from year-two

Figure 3.14 Camera sites relative to glacier surface

B. Field tests - Nisqually Glacier, Washington

Camera sites were established in the east wall of the Nisqually glacier valley about 600m apart, Figure 3.14. Each site was somewhat more remote than those of the previous field season, requiring longer hikes to set-up and access. Camera assemblies were enclosed in small tents with lenses directed toward the icefall area through the open front flap. Sturdy, lag-bolted, wooden stands, custom fitted at each site, held the camera bodies elevated at an angle of roughly 15 degrees from horizontal. At this angle, the lens rested about 0.3m above the hillside surface.

After delays caused by weather and recalibration of exposure and processing procedures, artificial field displacement tests, using Spectroscopic 649-F emulsion, proved successful. Fringe visibility produced from some images was adequate, the failures underscoring the necessity of precise focusing.

Simultaneous, time-lapse, double exposure experiments were initiated several times during the following week by operators communicating by radio. Environmental factors such as weather, influx of volcanic haze and dew on the lenses often delayed the second of the double exposures. With patience and luck, time-lapse experiments of 4, 24 and

48 hour intervals were completed (using the 649-F film, F#16, 2s each exposure).

There was no apparent motion on the 4 hour, double-exposure plate; no fringe patterns were produced. This result was similar to results of earlier 4-hour experiments conducted during year-one field study. Similar also to year-one results, the 48 hour test images exhibited excessive camera motion which obliterated speckle correlation.

Twice, simultaneous, 24 hour tests were conducted under good conditions. A bookkeeping error left one plate uselessly overexposed while the other three, upon cursory inspection, showed good exposure and focus. Two plates, recorded simultaneously from different sites, are reproduced in Figure 3.15. Careful inspection reveals the slight change of perspective between the two. In the field, fringes appeared to be marginally visible. It was assumed, however, that in the laboratory, visibility would be much improved.

Theodolite surveying was conducted during the double exposure experiments. Distinctive features found on the glacier surface images were located with respect to the camera sites and to existing surveying markers. These markers were precisely located during a previous surveying expedition [28] and appear on official USGS maps of the area.

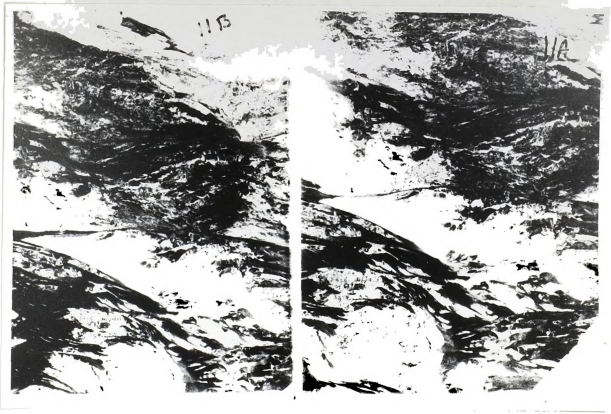

Figure 3.15 Prints from 24hr stereo plates, year-two

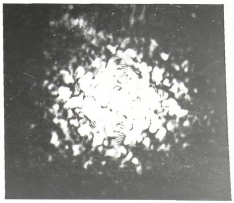

Figure 3.16 Fringe patterns from rock strata, Ptarmigan Glacier valley wall (fringe bands extend from upper left to lower right)

Satisfied with the three twenty-four hour plates, and with the field work still on schedule, the research team considered taking a chance on the weather and moving the expedition to the Ptarmigan glacier near Juneau, AK. Weather in southeast Alaska is indeed unpredictable. Ascending rapidly up the slopes of the Alaskan icefield, moisture is squeezed from the prevailing sea-borne winds over the cities from which the weather reports had been obtained. In the summer of 1982, however, reports of rainy, overcast periods had been surprisingly few. Deciding to continue according to the original research plan, the field team pressed ahead with experiments in Alaska.

C. Field tests-Ptarmigan glacier, Alaska

Experiments on the Ptarmigan were delayed. Luck had apparently worn thin as poor weather kept the field team's helicopter grounded for several days. Finally, the overcast lifted long enough to allow transport. Once on the glacier feeding icefield, two camera sites were established on the east Ptarmigan glacier valley wall. Camera stands and tents were well anchored. Environmental changes again forced recalibration of experimental procedures. Cooler ambient temperatures changed exposure times and unheated buildings required development of new cold-processing methods. Artificial field displacement tests were not immediately

successful, again because of poor weather (i.e. near white-out conditions).

Close examination of the first artificial field displacement plates, shot through the mist, revealed unexpected results. Fringe patterns were produced from a rock strata image, the strata being located across the glacier valley from the camera sites. The vertical, ice-carved wall did not appear to have great contrast compared with the adjacent glacier surface. Nevertheless, noisy fringes, as shown in Figure 3.16, were generated across much of the rock strata image.

A sudden, mid-morning clearing allowed successful completion of artificial displacement tests. A 24-hour, time-lapse experiment was quickly initiated. Benign weather transformed, within hours, to 60 knot winds and white-out conditions. Westerly wind-driven hail pummeled the aluminum clad encampment huts for the next two days. As workers ventured out to check the status of the equipment, one camera was found being dragged about by a shredded, billowing tent. With moisture covering the lens of the other camera and no break forecast, it was decided to abort the experiment. Despite the effort, no ice flow data was collected during the Alaska sojourn.

After packing the photographic equipment and making ready for the end-of-season closing of the icefield encampment,

members of the research team waited for two days until the white-out lifted sufficiently to allow the helicopter pilot to locate the camp. Giving the field team a final impression of its fickleness, the weather rapidly closed in again, stranding the team for an additional overnight. Late the next afternoon, all fled the icefield just as the long winter set in, ending the 1982 field season.

D. Fringe pattern analysis

Detection and analysis of Young's fringe data of the second field season differed from methods of the first year because of substantial equipment changes, mentioned above. Young's fringe patterns were transformed into ice surface velocity maps in order to compare the new results to those of the previous year, and to flow rate information gathered by conventional methods. This comparison was made in order to compile a list of recommendations aimed at increasing both precision and facility and to determine the merit of full-scale development of the new optical technique.

Photoplates, double exposed over 24 hour intervals at the Nisqually glacier, were analyzed in the steps enumerated below. General similarity exists between the analysis methods used following the two field seasons. Differences are presented in detail.

(1) Laboratory detection of Young's fringe patterns, generated from each of the three successful plates, was more difficult than anticipated. Diffraction efficiency of the Spectroscopic emulsion, when used in the specialized cameras, was poor. In visual comparison to plates of the previous year, less contrast was evident. Duplication of the recent plates on more 'contrasty' holographic emulsion, by a method identical to contact printing, resulted in improved fringe visibility when the reproduced film was interrogated. Compressing many gray tones into few, this process left the duplicates overexposed in some areas and underexposed in others. Using the common darkroom practice of 'dodging', however, it was possible to partially compensate for mis-exposure on both the duplicate and the original.

When this duplication process did not increase fringe visibility (on areas of glacier surface image thought necessary for good coverage), mechanical oscillation of the duplicate image, during the interrogation process, was often helpful.

In-plane vibration of the 4x5 film, at 50-60Hz and at an amplitude of about 5mm, spatially averaged optical noise. This process is somewhat akin to autocorrelation of temporal data to filter low level, periodic signals from noise. Temporal autocorrelation makes use of the random nature of

noise; after sufficiently long time period, this mathematical process ensures that random signals cancel one another, whereupon the previously camouflaged period of the desired signal becomes evident. The space oscillation process, on the other hand, does not reduce 'noise'. Since speckle cell pitch does not vary significantly over the 5mm range of motion and 'noise' does vary, the visibility of the once-masked signal is enhanced. The fundamental difference in the two signal enhancement techniques lies in the one-sided nature of light as opposed, for example, to the positive and negative displacements of seismic signals; there is no such thing as a light diode. With oscillation, many stubborn image points finally yielded Young's fringe patterns of adequate visibility.

Maximum spatial frequency of the artificial field displacement tests glacier images were again inferred from the size of the diffraction halo. Based on the 12mm halo diameter (using eqn. (2.26b)), the finest spectral components were about about 4.8 lines/mm. The 24 hour, time lapse images exhibited virtually the same maximum frequency. Reasons for obtaining relatively low resolution in outdoor conditions are discussed in Chapter 4.

With fringe bands visible, information required to determine net ice displacement was gleaned from each photoplate in much the same fashion as in year-one:

(1) Fringe separation and fringe axis data were logged at several points of the glacier surface image. Fringe axis minima spacing within the 24-hour-test halo varied over the image from roughly 5 to 10mm. Location of the fringe generating points, in image plane coordinates, was also recorded at this time. The vertical reference direction was taken as the top edge of the photoplate, which had been leveled it may be recalled, before exposure. Using data gathered by theodolite, points on the image where fringe patterns were logged were located on the topological map of the glacier surface. Surface normals were estimated at nine of the points, giving the best coverage across the glacier area of interest. Using eqn. (1.1), a gross displacement vector was calculated corresponding to each of the nine points.

(2) In a manner similar to that of year-one analysis, rigid body motion was detected by microscopic examination of the processed photoplates. Two 'rigid body' points, appearing in each image, were examined for spurious movement. Displacement vectors at each point were estimated with a finely graduated scale and protractor. Finally, location, in image plane coordinates, of each 'rigid body' point was noted.

(3) A specially written computer routine (revised from year-one) vectorially subtracted rigid body motion from

gross displacement at each generating point on the image. The Euler angle algorithm, described above, calculates a unique rigid body displacement vector for each image point. The appropriately scaled rigid body displacement was then subtracted from gross displacement at nine of the points logged in step (1), giving net ice displacement for nine points on the glacier surface image.

(4) Also in a manner similar to year-one analysis, each net ice displacement vector was scaled according to magnification and then projected onto the glacier surface.

(5) The stereo camera system allowed direct comparison of results when the two resulting velocity maps, from data acquired simultaneously, were superimposed. The merged velocity maps did not appear to coincide. If errors were due to mis-estimates of rigid body motion, then small, appropriate adjustments of the original measurements would bring about convergence. In an iterative (and admittedly, partly intuitive) process, small, incremental changes in both magnitude and direction of rigid body vectors were made on each plate. (The computer code for this exercise appears in Appendix 2.) Alternately repeating steps 3 through 5 on each plate brought about rough correspondence.

Figure 3.17 shows this 'boot-strap' process graphically for one of the 24 hour plates. Consider the nine sets of three

vectors originating from common points on Figure 3.17. Each vector set is shown in proper relation to the others in glacier surface coordinates. Within a set, each vector indicates,

(1), the ice flow field resulting from raw data (gross ice displacement with no rigid body correction, marked N),

(2), raw data with rigid body correction (gross ice displacement with rigid body correction, marked R), and

(3), raw data with a forced rigid body correction (marked F).

The vector drawn from the tip of N to the tip of F is the unique, effective, forced rigid body correction for each glacier surface point. Corresponding diagrams gleaned from the other, simultaneously recorded 24 hour plate are similar.

III. SUMMARY - EXPERIMENTAL RESULTS

Figure 3.18 is a plan view of the Nisqually Glacier surface showing the location and relative magnitude of 'forced solution' ice surface displacement during a 24-hour period in late August, 1982. Nine flow vectors were gleaned from each of two, simultaneous, double-exposed, high resolution photoplates. For comparison, the results of year one and the one nearly-overlapping point from Hodge [28] are included. Results from each study are in good agreement.

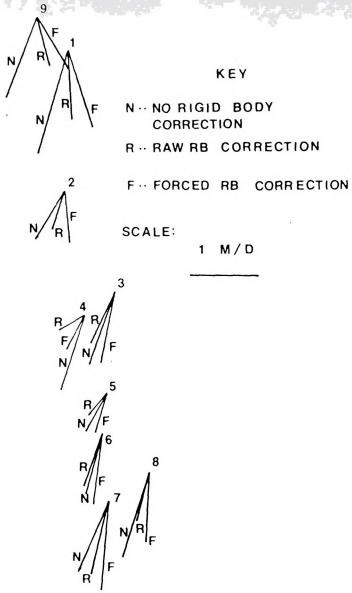

Figure 3.17 Ice displacement results from one of the year-two stereo plates showing 24hr ice displacement with: no rigid body correction, raw rigid body correction and forced rigid body correction

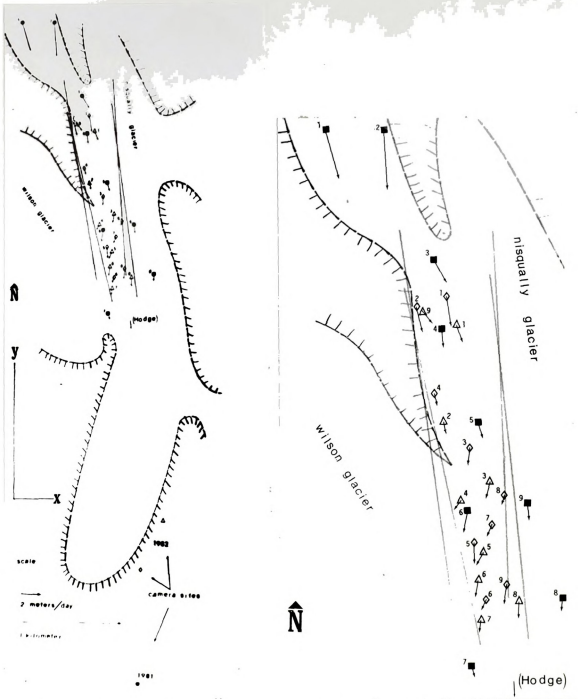

Figure 3.18 24hour Nisqually ice displacement for years -one (marked ■) and -two (marked ◇ and △) field seasons with one comparison point from Hodge [28]

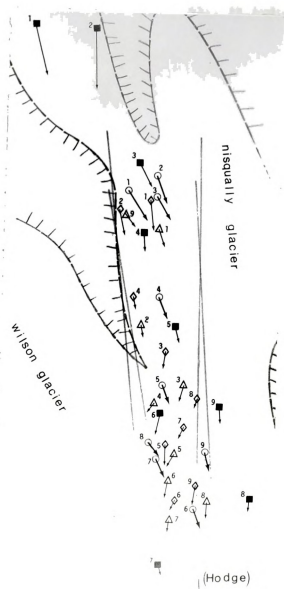

Figure 3.19 Repeat of Figure 3.18 with results (marked ◯) from single plate (whose mate was lost)

The third photoplate (whose mate was lost), was analyzed in the same manner as above, stopping short of the step 5 comparison/compromise. General agreement with the 'forced', simultaneous solutions is satisfactory, as seen in Figure 3.19.

Tabulated ice displacement components for 24 hour intervals, gathered from each of four photoplates, is given in Table 3.1 which follows.

TABLE 3.1

ICE DISPLACEMENT COMPONENTS FOR 24HR INTERVAL-NISQUALLY

in meters/day (rounded off)-refer to Figure 3.19

symbol	■	△	◇	○
		stereo-pair		
point no.	year-one X,Y,Z magnitude	year-two X,Y,Z magnitude	year-two X,Y,Z magnitude	year-two X,Y,Z magnitude
1	0.6,-2.1,-1.2 2.5	0.2,-1.3,-0.5 1.4	0.3,-0.8,-0.4 0.6	0.6,-1.4,-0.8 1.8
2	0.2,-2.6,-1.5 3.0	0 .3,-1.1,-0.5 1.2	0.1,-0.4,-0.4 0.6	0.4,-1.2,-0.8 1.5
3	0.1,-1,-0.6 1.3	-0.1,-0.7,-0.3 0.8	-0.2,-0.7,-0.4 0.5	0.6,-1,-0.7 1.3
4	0.1,-0.7,-0.5 0.9	0.1,-0.4,-0.2 0.5	-0.3,-0.4,-0.1 0.5	5,-1.1,-0.6 1.3
5	0.2,-0.6,-0.5 0.8	0.0,-0.8,-0.4 0.9	-0.2,-0.4,-0.2 0.5	0.4,-1,-0.6 1.2
6	-.2,-1.0,-.4 1.1	-.2,-.4,-.2 0.5	-.1,-.9,-.4 0.8	.4,-1.0,-.5 1.2
7	.2,-.6,-.2 0.6	-.2,-.5,-.2 0.6	-.1,-.9,-.4 1.0	.4,-.9,-.5 1.1
8	.0,-.5,-.3 0.6	-.1,-.3,-.1 0.3	.0,-.7,-.3 0.8	.4,-.5,-.5 0.8
9	.1,-.9,-.4 0.9	-.1,-1.0,-.2 1.1	.4,-.5,-.4 0.7	.3,-.9,-.6 1.1

CHAPTER 4

DISCUSSION AND CONCLUSIONS

I. IMAGING SYSTEM RESOLUTION

Sensitivity of the speckle-interferometric method is fixed by the minimum recorded speckle size. Limiting the spatial frequency of the specklegram image simply limits the minimum displacement that can be detected. In the case of pointwise filtering, however, truncated specklegram frequencies contribute also to a 'fringe shift' as noted in Chapter 2. Fringe axis shift partially masks the actual location of the cosine-squared extrema, resulting in measurement errors. Thus it is important to identify the causes and extent of frequency truncation.

To this end, consider the apparent resolution of each camera system used in this study. Each design appears to image different maximum frequencies for different conditions. It will be helpful to compare the imaging characteristics of each instrument. A common parameter describing the performance of astronomical telescopes, 'angular resolution', will be adopted. This parameter is often expressed in arc-seconds (1 degree = 3600 arc-seconds). Angular resolution of the cameras used during each of the two field seasons, under various imaging conditions, is

given below. Resolution values are given by theory or inferred from either bar chart tests or from diffraction halo size as described in the following paragraph. The results are compiled in Table 4.1.

For a circular aperture system, recall that the theoretical maximum image plane spatial frequency is, repeating eqn. (2.18b), $u_{max} = 2a/\lambda R$. Here, a is aperture radius, λ is the average noncoherent wavelength of the illumination, taken here as 6x10-4mm, and R is the focal length of the imaging lens. But, since $2a/R = 1/F\#$, then $u_{max} = 1/\lambda F\#$. Thus, the maximum theoretical angular resolution, γ, is

$$\gamma \approx \arctan\left(\frac{1/u_{max}}{R}\right) \qquad (4.1)$$

$$= \arctan\left(\frac{\lambda F\#}{R}\right) = \arctan\left[\frac{6F\#}{(10E+4)(R)}\right]. \qquad (4.2)$$

Equation (4.2) is used to calculate the maximum theoretical angular resolution entered on the first line of Table 4.1. In order to calculate the values entered on the second line, eqn. (4.1) is combined with the values of the maximum spatial frequencies transmitted by the camera lenses during optical bar chart tests. Equation 4.1 is combined with the maximum spatial frequencies inferred from halo diameter (as reported in Chapter 3) to calculate the remaining two lines.

TABLE 4.1

SPECTRAL RESPONSE OF IMAGING SYSTEMS FOR VARIOUS CONDITIONS
in arc-seconds; emulsion and test parameters noted

	YEAR-ONE 500mm lens	YEAR-TWO 916mm lens
Theoretical maximum - using eqn. (4.2)	2 @ F#8	2.2 @ F#16
Practical limit - (4.1); bar chart test results	3 @ F#8	3.1 @ F#16
Artificial field displacement tests of parking lot surface, using (4.1); inferred from diffraction halo size	(13 @ F#8)*see text 16 @ F#11, 1/8s 22 @ F#22, 1s each exposure Holo-film SO-253	11 @ F#16 2s each exp Spectro-plate 649-F
Artificial field displacement tests on glacier surface, using eqn. (4.1) (inferred from halo size)	52 @ F#16 1/50s each exp Holo SO-253	47 @ F#16 2s each exp Spectro 649-F
24 hour time lapse test on glacier surface, using eqn. (4.1) (inferred from halo size)	50 @ F#8 1s each exp Spectro 649-F	47 @ F#16 2s each exp Spectro 649-F

Note that all year-two experiments were carried out at F#16, the glacier imaging setting. Imaging at many different settings is evident, on the other hand, during year-one experiments where a variety of emulsions were used. Despite this diversity, it is possible to compare the performance of each camera type at constant F#. This means that the performance of the year-one instrument was inferred from the results of the artificial displacement tests in which the graveled parking lot surface was used as the object. It can be seen that the angular resolution for this set of experiments became finer as the aperture increased two F-stops in diameter from F#22 to F#11. This behavior was anticipated. Furthermore, an additional increase in resolution would be expected if the same scene had been recorded at F#8. Unfortunately, no such experiment occurred; the results of such a test may be estimated, however. It is reasonable to assume that if two F-stops reduced the angular spread by 6 arc-seconds then one additional F-stop would reduce it linearly by an additional 3 arc-seconds. Thus, it can be assumed that, had the specklegram been recorded at F#8, the resulting angular resolution would prove to be about 13 arc-seconds. This estimated value is denoted in Table 4.1 with an asterisk.

Holographic and Spectroscopic emulsions were both used in the photography experiments summarized above; these coatings have comparable resolution but spectral sensitivity of the

Spectroscopic emulsion is somewhat more broad. Recall that duplication of the Spectroscopic plate onto more contrasty Holographic emulsion was required during year-two experiments in order to increase diffraction efficiency. Spectroscopic emulsion was used during the first-year, however, with good results upon filtering the primary plate. The difference is the coated lenses used in the year-one experiments. Stray reflected light reduces image contrast. This is especially true of highly corrected instruments having a large number of air-glass surfaces; lens coating substantially reduces internal reflections. It may be concluded that coated lenses render images having higher diffraction efficiency, especially when the image is recorded on emulsion having broad spectral response.

Summarizing Table 4.1, it is seen that the resolution limit of the year-one and year-two camera lenses is approximately equal for equal conditions regardless of emulsion. The resolution limit, as determined from the indoor bar-chart tests should be taken as a relative measure between the year-one and -two systems since the eye perceives greater detail than that which could actually be imaged by the lens. The three arc-second limit, nevertheless, fits nicely between the theoretical value and the values determined from artificial displacement tests.

There is noted, however, a significant resolution reduction when shooting at equal distances outdoors rather than indoors. Recall optical bar-chart tests were conducted indoors at a distance of 130m for the year-two camera, while artificial displacement tests, using the same instrument outdoors, were conducted with about the same camera-to-object distance (about 150m). It was assumed that virtually all spatial frequencies appeared across the surfaces of both the parking lot and glacier-with proper lighting. Evidently, refraction gradients in the media through which the images were collected affects the spectral components in such a way as to act as a low pass filter. This effect is known in astronomy as the 'seeing' limit.

In order to determine this upper frequency bound, some background is necessary. In a landmark work related to stellar signal distortion, Fried [54], explains that the incoming wave front is 'tilted' by turbulent media through which the front must pass (i.e. tilt is a function of time). "Tilt displaces the image but does not reduce its sharpness. If a very short exposure image is recorded, the image...is insensitive to tilt, which can be a substantial part of the total distortion". An isoplanatic column of air through which two nearby beams travel to the imaging lens varies with space and time. Refraction characteristics of such a column are considered constant for a 'short' time interval. Short time exposures for astronomical imaging range up to 20

milliseconds, with most workers using exposure intervals of less than 10 milliseconds [53]. The minimum glacier exposure interval was equal to the larger value, but most photographs were recorded at much longer exposure times. Wave-front tilt, evidently, caused spurious, high-temporal frequency image oscillations. These were first noted during outdoor artificial field displacement experiments. Images collected outdoors are assumed to be distorted by wave-front tilt and the spatial frequency band was clipped by an amount proportional to the level of turbulence.

Astronomers characterize this complication by multiplying the telescope modulation transfer function (MTF) by a 'structure' function which describes the wave-front perturbation statistics in the entrance pupil. Some researchers [54] feel that such a procedure is an oversimplification, that is, lens and atmospheric effects cannot be separated in the manner such theory suggests. Alternative viable theories, however, are simply unavailable. For the present, workers must cast about within the sea of speculation to find a suitable multiplying function. Such a technique is used below. In applying this theory to the present work, it is assumed that a 'suitable' frequency-dependent ratio term simply diminished image plane intensity of the higher spatial frequencies (i.e., the term multiplies eqn. (2.15)).

Von der Luhe [57] uses the results of Korff [55] to describe the wavefront statistics and then computes the ratio of the squared-MTF's, with and without atmospheric turbidity. The analysis is centered about a very narrow optical frequency range of wavelength 4.4x10E-4mm. Some of von der Luhe's theoretical results are shown (dashed) in Figure 4.1. The horizontal axis is the non-dimensionalized, relative spatial frequency, w/w_{max}, where w_{max} is the maximum theoretical limit admitted by the aperture (given by eqn. (2.18b)). The numbers next to each curve are the values of the parameter, $\alpha = r_o/D$, where D, is the aperture diameter, and r_o is an atmospheric turbulence parameter, the latter first suggested by Fried [54]. In order to make use of von der Luhe's results, r_o must be determined. Unfortunately, very little is found in the literature related to daytime 'seeing' extended objects through a finite atmospheric layer of nearly constant altitude. Astronomers feel that most of the stellar signal distortion occurs during its passage through the lowest level of atmospheric layers [27] so a stellar model may adequately account for the perturbations incurred by terrestrial waves recorded in the present study. Viewing angle inclination and station altitude [57] also affect 'seeing'. Thus, a stellar imaging model that accounts for inclination is sought. Hufnagel's turbulence model [56], abstracted in Figure 4.2, is one such prototype. At an altitude of 10m (glacier images were shot low over both the

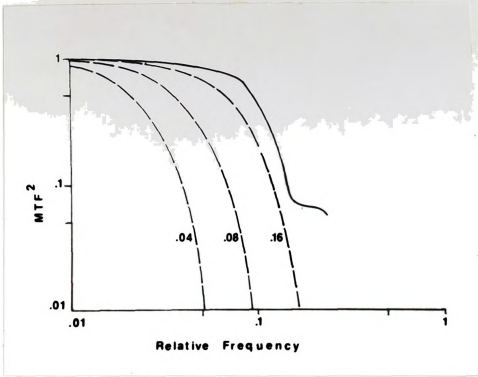

Figure 4.1 Modulation transfer function for atmospherically degraded images-abstracted from von der Luhe[58]

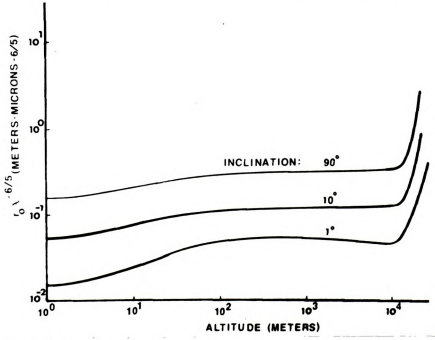

Figure 4.2 Hufnagel's atmospheric turbulence model-abstracted from Korf [56]

glacier valley and over the glacier surface), for λ = 0.5x10E-6m (= 0.5 microns), and an inclination of 1 deg., Hufnagel's model gives,

$$r_o \lambda \exp(-6/5) = .02.$$

Thus, $r_o \approx$ 9mm. The parameter $\alpha = r_o/D$, for D = aperture diameter = focal length/ F-number, is ≈.15. Interpolating the appropriate curve of Figure 4.1, it is seen that fringe intensity is reduced to .5 of its zero frequency value at a relative frequency of .06. For the year-two study, this means that the angular resolution is about 1/.06 ≈ 17 times coarser than the theoretical minimum of 2.2 arc-seconds. Thus atmospheric cut-off is predicted to be about 37 arc-seconds. The same analysis predicts significant clipping begins at angular resolution less than 40 arc-seconds for the year-one camera. Discrepancies may be the result of von der Luhe's single frequency analysis as opposed to the relatively broad-band, visible light domain used in the present study. Nevertheless, correspondence between these numbers and the last entries in Table 4.1 is very good.

Von der Luhe's work is cited because it is recent (1984) and because he included experimental results which were garnered from a large number of solar observations at the Mt. Palomar Observatory. It is worth noting that the theoretical attenuation, plotted (solid) for different α's, seem to

collapse, upon experiment, into the narrow range shown dashed in Figure 4.1. This behavior is due, von der Luhe explains, to experimental error. Using von der Luhe's experimental results and again assuming cut-off is where intensity falls to .5 of maximum, predicted angular resolution is about 30 arc-seconds for each camera system. Again, this value corresponds reasonably well with the resolving power demonstrated at the glacier site.

Discrepancies between these results and those of von der Luhe's could result from mis-focus. It is shown (in Chapter 2.I.C) that the glacier instruments, for example, require focus adjustment accurate to about .5mm. Thermal expansion or other dimensional changes beyond the control of the operators may have changed the focal setting and thus exceeded this bound. The relatively low and narrow frequency range imaged at the glacier sites tends to minimize the effects of defocus. Thus, one of the advantages of atmospheric clipping is less stringent focusing requirements.

Off-axis contrast losses may have a somewhat stronger effect than mis-focus. Image points located far from the optical axis have been gathered from object points which lie outside the central isoplanatic patch; the MTF depends on field angle. Since the point spread function is not radially symmetric (as is usually the case except on the axis) the

MTF will also vary with azimuth of the object lines defining it [37]. This is the sum effect of aberrations.

It is difficult to quantify this behavior in the glacier imaging cameras. When scanned along a radius, the specklegram images produced fairly constant halo diameter, indicating constant spatial frequency. The problem may simply be one of measurement; a few mm change in the location of an ill-defined boundary is not easily discerned. Real lenses, however, (see any technical performance report on quality photography equipment) show a contrast loss in the range of 20 to 30% from center to edge for most F#'s. Since the glacier flow data was gathered from points far from center of the specklegram image, some additional losses can be expected (even though such tests of popular camera equipment are conducted at wider angles). It is concluded that data gathered from the image center would generally exhibit higher spatial frequency and thus be in closer correspondence with von der Luhe's results.

Finally, it is noted that the results of the present study are in the range of Worden's assertion [53] that a roughly 50-fold reduction in angular resolution is expected from the theoretical limit when imaging starlight through the atmosphere.

With so many parameters available, it might be argued, a moderate correspondence with all the data was inevitable. Struggling against the paucity of facts related to terrestrial imaging the agreements are, nonetheless, pleasing.

For completeness, another technique allowing measurement of motion which would otherwise be too small is noted here. The method consists of displacing the camera a known amount between exposures, in the plane of the film. Thus, object motion is added to camera motion in the specklegram record. During analysis, the prescribed camera motion is then subtracted from the gross image displacement in the manner given in Chapter 3. Rendering object displacement (referred to the film plane) in an acceptable range by intentional movement of the camera has been successful in the laboratory [13]. It is anticipated that this technique can be adapted to other geophysical problems and to other large dynamical systems.

While atmospheric effects may limit resolution even in good weather, sufficient information can be recorded (on relatively inexpensive film) to determine displacements if the time interval between double exposures is properly selected.

II. ERROR ANALYSIS

Capturing fringe-generating glacier images was the objective during the year-one field season. Accordingly, parameters such as vertical reference direction, rigid body displacement reference point location, topological map location of glacier surface features, and other data were not precisely determined during the first Nisqually visit. Flow rate error estimates for the year-one experiments were difficult to generate. Such estimates are given below for the year-two study, however, with a closing note comparing the results from the two field seasons.

Errors are introduced at three stages in the interferometric measurement process. Each, in turn, is discussed below; the accumulated errors are estimated in the final section.

A. Fringe pattern measurement

In an effort to increase speed and accuracy of an otherwise tedious exercise, electronic devices such as diode arrays and computing machines have been recently adapted to the fringe measurement task. An important parameter in the automated process is fringe visibility which, in this case, is easily quantified. (Visibility is defined and discussed with respect to the pointwise filtering method in Chapter 2.IV.B.) The manual (visual) method used in the present

study, however, does not include quantification of this parameter. In order to determine the effects of fringe visibility the value must be estimated; 0.4 seemed reasonable. In the range of visibility from 0.3 to 0.5, and with three (or perhaps more) fringes in the diffraction halo, Kaufmann's analysis [51] predicts the distance between apparent fringe minima will measure 10% to 15% greater than the true value. Accordingly, the resulting uncertainty in the measurement of fringe minima separation distance is about 5%. Because, according to eqn. (1.1), film plane displacement is linear with fringe separation, the gross ice displacement estimates are also ±5% uncertain owing to poorly specified visibility.

Interferometry reveals not only magnitude but also direction of the displacement occurring between exposures. It has been found that such direction (fringe axis orientation) measurements, with practice and patience, were repeatable to within ±2 deg.

B. Rigid body motion determination

Relative motion of the camera with respect to the object surface is viewed as the single most important factor affecting accuracy. As indicated in the previous chapter (3.VI.C), such motion is detected with photogrammetry

methods. Thus, interferometric measurements were degraded to the lower confidence level of the photogrammetry process.

Microscope measurements of the displacement of 'fixed' points in the image yield the so-called 'rigid body displacement' vectors. Magnitude estimates of these vectors by different members of the research group are repeatable to ±20%, while orientation estimates vary in the range of ±5 deg. These potential errors are not as important, however, as are the differences between the initial rigid-body motion estimates and the final values arising from the forced simultaneous solution. Recall from the previous chapter that associated with each point on the photographic image there is: (i) a unique gross displacement inferred from fringe patterns; (ii) a unique rigid body displacement (calculated from Euler angle parameters and original rigid body estimates); and, (iii) a unique rigid body displacement vector that corresponds to the final forced solution. As seen in Figure 3.17 (Chapter 3.II.D), it is clear that final rigid body motion vectors do not, on the whole, vary largely from the original estimates. Indeed, the differences in both magnitude and direction are within the previously stated range of ±20% and ±5 degrees.

Means to improve precision by delineating the rigid body motion interferometrically in subsequent field tests are proposed in the final section.

C. The projection of net ice displacement onto the glacier surface

Here, the critical value is the glacier surface location corresponding to the image point at which fringe patterns were detected. Optical magnification and geometric projection of net ice displacement onto the glacier surface is strongly dependent on these coordinates. During year-two field work, careful surveying located such glacier surface points to within a few tens of meters. Magnification was easy to calculate within a fraction of a percent.

The larger problem was to estimate the surface normals on what is a highly convoluted surface. Determination of an 'average' slope turned out to be fairly straight-forward since lasers used in the pointwise filtering process produce 2-3mm diameter beams which subtend a relatively large area of glacier. This area corresponds to an ellipse, when projected onto the glacier surface, which is roughly the size of a football field. Since spatial frequencies are averaged over precisely the same elliptical area, 'average' surface slope estimates are justified.

Topological maps show Mt. Rainier's south flank varies, on average, between 27 and 38 degrees from horizontal, gradually decreasing toward the Nisqually snout. Over a distance of 40 to 50 meters (the maximum surveying error),

the slope does not change more than 3 degrees; average slope values are, therefore, accurate to at least ±3 degrees, with the same confidence in average surface normals.

Though topological maps were compiled from eight-year-old data, general features such as surface slope and icefall location, do not change dramatically over time. For the present purposes then, use of 'old' maps contributed negligible error.

The computer algorithm (shown in Figure 3.10, and documented in Appendix II) projects net ice displacement whose magnitude is proportional to the cosine of the surface normal. Using the given error limit, the ratio of possible cosines gives the maximum ice displacement magnitude error. Near the icefall the surface normal is about 52 degrees from horizontal. With ±3 degrees confidence in the glacier surface slope values, the ice displacement may vary about,

$$[1 - \frac{\cos(52)}{\cos(52\pm3)}] \times 100 \approx \pm7\%.$$

Thus, near the maximum slope, ice displacement rate errors are no more than ±7% in magnitude. A similar calculation for down-glacier points, where the slope is about 27 degrees, gives about ±10% maximum error.

D. Accumulated errors

Vector magnitude errors incurred in each of the analysis stages are multiplicative; their handling is straightforward. Angular measurement uncertainties, however, are coupled to vector magnitudes because of the projection of the image vector domain (a circle) onto the glacier surface ice displacement range (an ellipse). For the relatively small angle measurement errors of the present case, such coupling can be ignored. Angular uncertainties are thus additive. The possible range of azimuth for any of the ice displacement rate vectors shown in Figure 3.18 is thus,

$$\pm(2 + 5) = \pm 7 \text{ degrees.}$$

Using the possible measurement errors characterized in the three previous sections, ice flow rate magnitudes may vary up to

$$1 - (1\pm.05)(1\pm.20)(1\pm.07) \approx \begin{matrix} -30\% \\ +35\% \end{matrix}$$

from their given value for up-glacier regions. For down-glacier areas, the possible error is,

$$1 - (1\pm.05)(1\pm.20)(1\pm.10) \approx \begin{matrix} -32\% \\ +39\% \end{matrix} .$$

These discrepancies are roughly in the range of seasonal variations reported by Hodge [28] who, using conventional methods at the same glacier, measured flow rates varying about 25%.

Though the above analysis addresses year-two results only, good comparison between the flow data from the two field seasons indicates that year-one errors are of similar size.

III. COMPARISON OF RESULTS WITH ICE FLOW THEORY

At the current level of development, the theory of ice flow is not adequate to describe the behavior of real ice in either ice sheets or glaciers. Nye [33], Patterson [34] and, more recently, Hutter [35] are among many who offer versions of ice rheology in naturally occurring bodies. With time, succeeding theories have understandably become more complex and more in need of field data to fix boundary conditions and to establish phenomenological relationships. The boundary-value problem, coupled with temperature and velocities defies exact solution. Also, it is difficult to identify trends from numerical results, which are inherently over-specific. The problem is classic: there are simply too many unknowns to allow a general analytical solution.

As an illustration, consider the ice flow formula developed by Patterson [34]. Using Glen's [25] flow law (i.e.

stressrate = A x strainrate^n, where A and n are constants), Patterson attempts to describe the simplest case of down-slope, laminar velocity for a deforming infinite ice sheet by the following formula:

$$U_s - U_b = 2[A_o \exp(-Q/RT)](\rho g \sin(\alpha))^n \frac{h^{n+1}}{n+1} \qquad (4.3)$$

The variables, with comments on their range of values and possible relationship to the behavior of real glaciers are described below:

U_s and U_b are the longitudinal velocity components of the surface and base, respectively. These are assumed to be the only non-zero components. Note that eqn. (4.3) gives differential rates only; it contains no information on absolute surface velocity. In real glaciers, basal sliding varies over an enormous range [36], depending on water storage and efflux, bed obstacle size and spatial frequency, and whether the creep mechanism or the melt-regelation process is dominant. Accounting for bed topography requires detailed seismic, gravity or sonar studies. Such painstaking work is rarely done on a sufficiently large extent of glacier to be useful.

A_o is given as a constant but, in fact, depends on the grain size, ice impurity and crystal orientation [18].

Q is the activation energy for polycrystalline ice. Actually Q is temperature dependent, doubling in value from -250°C to +100°C, according to Barnes [38]. Barnes reports that Q seems to be a function of the extent of the liquid phase at the grain boundaries.

The temperature T is a function of both position and time in temperate glaciers where the effects of strain heating are significant [35].

R is the universal gas constant.

The bracketed term in eqn. (4.3) is actually the viscosity A in Glen's flow law. Ice responds to deviatoric stress by becoming softer; the bottom layers slide over one-another more easily than those above, resulting in high velocity gradients near the sole. Little has been reported regarding the non-Newtonian properties of glacier ice exhibiting strain-rate dependent viscosity.

Ice density, ρ, for glacier work, is usually taken as .9 times the specific gravity of pure ice. Values from borehole measurements [34] vary, however, from 0.85 to 0.91.

g is gravitational acceleration.

α is the angle of the mean slope upon which the ice slab model slides. This value varies, obviously, along the course of a real glacier.

The exponent, n, is usually taken as 3 for glacier work, but Raymond [36] has surveyed experimental results and

found that this number varies from 1.3 to 4.2, with a mean of about 3.2, and that it is a strong function of stress.

Finally, h is slab thickness, assumed to be constant for the above model, but not for the real case. Thickness of glacier ice is roughly proportional to the inverse of the slope; mountain flanks supporting glaciers often vary 10 to 20 degrees from head to terminus.

Not mentioned above, in relation to the slab model, are other factors affecting flow:

The effects of valley walls which, in the case of the Nisqually icefall, are presumably significant since this body is relatively narrow. Rock side-boundaries may retard flow by surface friction or accelerate flow by providing a liquid-ice interface through heat conduction from the surface [34]. Such a melting condition obviously contributes to a transverse as well as a downward (toward the sole) velocity component.

Real glacier flow is seldom planar, due in part to the so-called 'submergence' velocity. In the accumulation area (e.g. above 2200m elevation at Nisqually) ice flow has a downward velocity component estimated to be 5-10% [34] of the gross surface displacement vector magnitude. Emergence velocity in the down-glacier ablation zone is the reverse of this trend. Emergence is physically understandable; if it did not occur the surface would become ever steeper.

Average Nisqually surface velocity varies as much as 40% on a monthly basis, as reported by Hodge [28]. Other glaciers exhibit similar but more extreme behavior. A theory has been offered by Raymond [36] which correlates temporal variations of velocity with stress. Observations by Meier [49], furthermore, have indicated that internal deformation seems to be controlled by an 'effective' slope. In Meier's model, effective slope is a function of bed topography, bed slope and surface slope, the latter changing slowly with time.

Quantitative comparison of the results of the current study with ice flow theory is fruitless; by observing the general characteristics of the above model, however, some of the trends observed in the velocity map, Figure 3.18, can be explained. Points 1 and 2 of the year-one results are located near the steepest part of the Nisqually icefall. Eqn. (4.3) indicates velocity has a strong dependence on surface slope; the relatively high rates shown here are expected.

With other factors constant, general theory predicts that down-slope flow rates gradually increase in the accumulation area and gradually decrease in the ablation area. Emergence velocity contributes to this tendency and is seen to be zero near the equilibrium line which separates the accumulation

and ablation areas. This trend is generally borne out along mid-glacier as in Figure 3.18.

Little general theory has been offered regarding ice behavior in zones of confluence. The Nisqually and its major tributary, the Wilson glacier, meet just below the rock formation known as the Wilson Cleaver. Here, a distinct, westward flow trend which is not directly down hill is noted in Figure 3.18. This is possibly the result of the convergence of differential stress zones. The greater accumulation area of the Nisqually, in this maritime region, could account for higher stresses in this body compared with those occurring at the same elevations in the Wilson. The meeting of these two systems is accompanied by a strain-rate component corresponding to the direction of decreasing stress gradient.

The glacier flow results from the two field seasons are observed to be self-consistent. They compare well with the limited available field data collected by conventional means, and they seem reasonable.

IV. FURTHER STUDY

A. Increasing precision

Researchers endeavor to raise the density of information that is photographically recorded. Generally, this means increased resolution, but successful efforts to image yet finer detail must be accompanied by equally well-described camera motion. Precise determination of camera motion and techniques to make use of high object-spatial frequencies follows.

a. Interferometric determination of rigid body motion

Camera motion is probable during time-lapse photography; reduction of such motion would be effected by steady camera mounting. Metal stakes, driven into the earth would provide substantially improved support. Two means to delineate residual motion are suggested.

Appropriately patterned stationary grids placed in the viewfield would serve to generate Young's fringes during the interrogation process. Two focused grids, localized in the photographic image, would provide sufficient information to determine translation vectors and Euler angle values; camera motion, in the plane of the film, would be completely specified. The photogrammetry exercise of step 2 (in

Chapter 3.I.C) would thus be replaced by the more accurate interferometric method. Grids may be any contrasting pattern provided the spatial frequency is high enough to register small relative camera movement but not so high as to be affected by atmosphere/lens attenuation. Determining useable grid patterns and placement would require but a simple series of on-site experiments carried out concurrently with artificial displacement tests. A completely interferometric method would raise precision by at least an order of magnitude.

Apparent camera motion would be effectively reduced to zero if two sequentially recorded photoplates (each single-exposed) were superimposed in exact registration. As explained in Chapter 3, such a configuration is allowed by recording alternate images on reversed emulsion (i.e. through the glass). Superimposing photoplates in perfect registration requires patience, intuition, and perhaps, specialized three-degree-of-freedom mechanical positioning equipment. Success has been reported by Adams [32], using laboratory subjects; it should be adaptable to larger objects. 'Perfect registration is and ideal condition; remnant camera motion could be ascertained by a hybrid of the above two methods.

Another problem, which should be remedied by steady camera mounting, is worth noting here. Dew collecting on the

lenses often delayed glacier time lapse experiments. Muirden [58], writing for amateur astronomers, suggests that a long black-lined tube extending beyond the telescope lens will help prevent dew from forming. With sturdy mounting, and well-defined camera motion, the effects of wind on a large tube extending several diameters from the lens would not be of concern. In addition, if the camera mount is sufficiently stout, it should be possible to simply remove the dew mechanically.

b. Short exposure methods

A series of short exposures, optically processed, allowed Layberie [39] to resolve dual stars which were far closer than the normal atmospheric seeing limit. Since this 1970 milestone, astronomers have used short exposures times to 'freeze' atmospheric refraction. The ensemble of a large number of photographs yields detail approaching the telescope diffraction limit. Unfortunately for the present work, Layberie's technique yields displacements, not displacement rates. Very short exposure times, nevertheless, ought to freeze the effects of atmospheric turbulence in terrestrial images as well. Upon filtering such a short-exposure specklegram, refraction gradients will be manifest by spurious fringe axis separation. At the same time, the diffraction halo will appear larger, indicating increased resolution. The trade-off is classic: higher

resolution for more noise. A series of on-site, variable-exposure-time experiments would provide an indication of the necessary sacrifices in attaining higher resolution. Addressing once again the desirable characteristics of photographic emulsion, it seems clear that narrow band, high response is indicated. Photographic media must image a narrow frequency band to counteract the contrast reducing effects of both dispersion and uncoated lenses (if used) and to facilitate short exposure intervals.

It is expected that statistical treatment of large numbers of high resolution images, each having well defined camera motion, will yield accurate flow rate maps. The large number of images required for accuracy will not limit data processing. Comparing many images is now possible with computer-based digital imaging techniques. Further, with the anticipated accuracy of such systems, optical processing may not, ultimately, be required.

B. OTHER APPLICATIONS OF THE WHITE LIGHT SPECKLE METHOD

TIROS-1, launched in 1960, was the first in a series of weather satellites used to map conditions on earth. Crude vidicon images provided the first, long-term, birds-eye views of large scale cloud patterns. Many geodetic platforms followed TIROS-1 into orbit. ERTS images [21], for example, were used to monitor and predict glacial mass

balance of hydropower regions in Europe. LANDSAT [22] images were photogrammically analyzed in an attempt to determine ice flow through Canada's Baffin Bay connecting the Arctic and Atlantic oceans. Judging from available reports, however, interferometric methods have not been applied to geophysical mechanisms using platforms in space. One reason is resolution: At the present stage of development, electronic imaging does not preserve the requisite structure; interferometric techniques require primary 'analog' character. This limitation is expected to diminish as digital information packing becomes more dense and the information itself becomes more easily manipulated.

For the current level of electronic imaging sophistication, however, the space shuttle provides the means to record and recover primary photographic data. High-resolution photographs of glacier or sea ice, or of large land masses, are achievable; the above-detailed experiments have demonstrated that Young's fringe patterns, indicative of displacement and strain, can be generated from such images. Superposition of single-exposure photoplates would be the required technique in this case where the camera cannot remain stationary during the time-lapse interval. There are many additional benefits of a vantage point from space: The required photographic equipment is small, reliable, relatively inexpensive and has been proven easy to handle in weightless conditions. 'Overhead' is a much desired

perspective from which to record geological processes occurring on the earth's surface. Reliance on topological map data is reduced. It is clear that space platforms can greatly expand the potential of the noncoherent light method.

APPENDICES

APPENDIX I

PHOTO PROCESSING DETAILS

Kodak Emulsion	Developing solution, time (min.) @ 20C	Fixing time (min)
Minicard II Film SO-424	D-19, 8	10
Fast Holographic Film SO-253 Plate 131-02	HRP (2:1), 2	5
Spectroscopic Plate 649-F	D-19, 7	10
(cold processing @ 15C)	D-19, 15	20

APPENDIX 2

COMPUTER CODE - FORTRAN V

```
ccccccccccPROGRAM GLA27 ccccccccccccccccc
      DIMENSION P(13),D(3),WKAREA(68),A(3,3),S(3,1),A1(2)
     +,W(9,5),CHARA(9,5),CHAR(13)
      CHARACTER*1 0,NUM
      CHARACTER*5 PTNO
      CHARACTER*4 F1
      CHARACTER*8 FILE,CHARA,GAP,GAQ
      CHARACTER*12 ZZ1,ZZ2,ZZ3,ZZ4,ZZ5,GFIL
      CHARACTER*20 LAO
      CHARACTER*44 CHAR,LA1,LA2,LA4,SCALE,LA5
      OPEN(7,FILE='OUTPUT')
      PRINT '(''PROGRAM GLACIER27'')'
      PRINT '(''ENTER DATA FILE NUMBER'')'
      READ(1,'(A4)')F1
      NFLAG=0
      PRINT '(''IF YOU WISH NUMERICAL RESULTS ENTER L'')'
      PRINT '(''IF NOT, ENTER 0'')'
      READ(1,*)NFLAG
      FILE='DATA'//F1
      OPEN(5,FILE=FILE)
      READ(5,*)P1X,P1Y,TMAG,GP,Q1X,Q1Y,GQ
CCCCCCCC INITIALIZE GRAPHICS CCCCCCCCCCC
      GMA1=30.
      CALL INITT(480)
      GFIL='G GLA27'//F1
      CALL OPENTK(GFIL,IER)
      CALL DWINDO(-400.,388.,000.,600.)
CCCCCCCCCCCC DRAW POINTS AT CAMERA SITES CCCCCCCCC
      CALL MOVEA(0.,1070.)
      CALL CHARTK('*',.4)
      CALL MOVEA(220.,1600. )
      CALL CHARTK('*',.4)
9     SIGN=1
1     TMAG=SIGN*TMAG
      P2X=TMAG*COS(GP)+P1X
      P2Y=TMAG*SIN(GP)+P1Y
      T=TAN(GQ)
      R=SQRT((Q1X-P1X)**2+(Q1Y-P1Y)**2)
      TEMP1=1+T**2
      TEMP2=2*(-P2X-(T**2)*Q1X+T*Q1Y-T*P2Y
      TEMP3=(T*Q1X)**2+2*T*Q1X*P2Y
     +-2*T*Q1X*Q1Y-2*Q1Y*P2Y
     ++P2X**2+Q1Y**2+P2Y**2-R**2
```

```
      DISC=(TEM2**2)-4*TEMP1*TEMP3
      IF(DISC.LT.0)THEN
      SIGN=-1
      PRINT '('' DOES NOT CONVERGE-INITIAL DISPLACEMENT '')'
      PRINT '('' DIRECTION CHANGED IN SIGN. '')'
      GO TO 1
      ENDIF
      DISC=SQRT(DISC)
      Q2X1=(-TEMP2+DISC)/(2*TEMP1)
      Q2X2=(-TEMP2-DISC)/(2*TEMP1)
      Q2Y1+T*(Q2x1-Q1X)+Q1Y
      Q2Y2=T*(Q2X2-Q1X)+Q1Y
      RX=Q1X-P1X
      RY=Q1Y-P1Y
      A1X-Q2X1-P2X
      A1Y-Q2Y1-P2Y
      A2X=Q2X2-P2X
      A2Y-Q2Y2-P2Y
      RMS=RX**2+RY**2
CCCCCCCCCCCCCALCULATE ROTATIONS CCCCCCCCCCC
      A1(1)=ASIN((RX*A1Y-RY*A1X)/RMS)
      A1(2)=ASIN((RX*A2Y-RY*A2X)/RMS)
CCCCCCCC SELECT SMALLEST ALPHA-PLATE ROT ANGLECCCCCCC
      ALPHA=A1(1)
      TRANSQ=SQRT((Q2X1-Q1X)**2+(Q2Y1-Q1Y)**2)
      ALPHALT=A1(2)
      TRANSQALT=SQRT((Q2X2-Q1X)**2+(Q2Y2-Q1Y)**2)
      IF(ABS(A1(1)).GT.ABS(A1(2)))THEN
      ALPHA=A1(2)
      TRANSQ=SQRT((Q2X2-Q1X)**2+(Q2Y2-Q1Y)**2)
      ALPHALT=A1(1)
      TRANSQALT=SQRT((Q2X1-Q1X)**2+(Q2Y1-Q1Y)**2)
      ENDIF
CCCCCCCCCC CALCULATE TRANSLATIONS CCCCCCCCC
      TX=TMAG*COS(GP)
      TY=TMAG*SIN(GP)
CCCCCCCCC OPERATE ON EACH POINT CCCCCC
      DO 2 I-1,9
      READ(5,*)(P(J),J=1,13)
      DX-P(7)*COS(+P(8))
      DY=P(7)*SIN(+P(8))
CCCCCCCCCCCCCALCULATE ROTATION ABOUT POINTCCCC
      V1X=P(12)-P1X
      V1Y=P(13)-P1Y
      R2X=V1x*COS(-ALPHA)+V1Y*SIN(-ALPHA)+P2X
      R2Y=-V1X*SIN(-ALPHA)+V1Y*COS(-ALPHA)+P2Y
CCCCCC CALCULATE RIGID BODY DISPLACEMENT OF POINT CCCCCC
      RBX=R2X-P(12)
      RBY=R2Y-P(13)
CCCCCCCC CALCULATE NET ICE DIP. REL TO FILM PLANE IMAGECCCC
      XNET=DX-RBX
      YNET=DY-RBY
      FDISNET=SQRT(XNET**2+YNET**2)
CCCCCCCCCC ACCOUNT FOR OPTICAL MAGNIFICATION CCC
```

```
      OD=SQRT((P(1)-P(4)**2+(P(2)-P(5)**2+(P(3)-P(6))**2)
      OM=OD/91.7
      XNET=XNET*OM
      YNET-YNET*OM
CCCCCCC CALCULATE NET ICE DISP. MAG AND ANGLE REL TO FILMCCC
      PHI=ATAN2(YNET,XNET)
      DNET-SQRT(XNET**2+YNET**2)
CCCCCCC CALCULATE VALUES FOR LEQT2F CCCCCCCC
      SI=-ATAN2((P(4)-P(1)),(P(5)-P(2)))
      D(1)=DNET*COS(SI)*COS(PHI)
      D(2)-DNET*SIN(SI)*COS(PHI)
      D(3)=DNET*SIN(PHI)
      A(1,1)=P(0)
      A(1,2)=P(10)
      A(1,3)=PP(11)
      A(2,1)=D(3)*(P(5)-P(2))-D(2)*(P(6)-P(3))
      A(2,2)=-(D(3)*(P(4)-P(1))=D(1)*(P(6)-P(3)))
      A(2,3)=D(2)*(P(4)-P(1))-D(1)*(P(5)-P(2))
      (3,1)=D(1)
      A(3,2)=D(2)
      A(3,3)=D(3)
      S(1,1)=0
      S(2,1)=0
      S(2,1)=DNET**2
      M=1
      N=3
      IDGT=1
      IA=3
CCCCCCCC CALL IMSLS SUBROUTINE CCCCCCCCCCC
      CALL LEQT2F(A,M,N,IA,S,IDGT,WKAREA,IER)
CCCCCCC DRAW GLACIER DISPLACEMENT VECTOR CCCCCC
      X=P(4)*.1
      Y=P*5)*.1
      CALL MOVEA(X,Y)
      0='0'
      CALL MOVEA(X,Y)
      VLEN=SQRT(S(1,1)**2+S(2,1)**2+S(3,1)**2)*GMA1
      ANGLE=ATAN2(S(2,1),S(1,1))
      CALL DRAWR(VLEN*COS(ANGLE),VLEN*SIN(ANGLE))
CCCCCC WRITE POINT NUMBER NEAR ORIGIN CCCCCCC
      CALL MOVEA(X,Y)
      CALL MOVER(0.,7.)
      WRITE(NUM,'(I1)')I
      CALL CHARTK(NUM,.7)
CCCCCC WRITE OUTPUT INTO CHAR ARRAY CCCCCC
      W(I,1)=FDISNET*10
      W(I,2)=S(1,1)
      W(I,3)=S(2,1)
      W(I,4)=S(3,1)
      W(I,5)=SQRT(S(1,1)**2+S(2,1)**2S(3,1)**2)
      WRITE(CHARA(I,1),'(F7.6)')W(I,1)
      WRITE(PTNO,'(I1)')I
      DO 3 =2,5
      WRITE(CHARA(I,J),'(F7.1)')W(I,J)
```

```
3     CONTINUE
      CHAR(I)=PTNO//CHARA(I,1)//CHARA(I,2)//CHARA(I,3)
     +//CHARA(I,4)//CHARA((I,5)
2     CONTINUE
CCCCCCCCC WRITE DATA FILE NAME CCCCCCCCCCCCCC
      LAO='DATA FILE NAME:'// F1
      CALL MOVEA( 10.,500. )
      CALL CHARTK(LAO,1.5)
CCCCCC DRAW SCALE CCCCCCCCCCCCCCCCCC
      CALL MOVEA(60.,400)
      SCALE='SCALE-1 METER/DAY:'
      CALL CHARTK(SCALE<.9)
      CALL MOVER(10.,000. )
      CALL DRAWR(GMA1,0.)
CCCCCCC WRITE CHAR ARRAY ON SCREEN CCCCC
CCCCCCC LABEL OUTPUT CCCCCCCCCCCCCCC
      LA1='ROT OF PLATE (deg)&TRANS OF PLATE(cm)'
      WRITE(ZZ1,'(F8.4)')ALPHA*57.2
      WRITE(ZZ2,'(F7.4)')TMAG
      WRITE(ZZ3,'(F7.4)')TRANSQ
      CHAR(12)-ZZ1//'PtP'//ZZ2//'PtQ'//ZZ3
      CALL MOVEA(05.,375)
      CALL CHARTK(LA1,.950)
CCCCCCCCCC WRITE CURRENT VARIABLES CCCCCCCCCCCCCCC
      WRITE(GAP,'(F7.4)')GP
      WRITE(GAQ,'(F7.4)')GQ
      CALL MOVEA(0.,325.)
      LA5-'GammaP='//GAP//' GammaQ'//GAQ//'(radians)'
      CALL CHARTK(LA5,.9)
      CALL MOVEA(00.,350)
CCCCCCCCCC WRITE ALTERNATE ALPHA AND TRANSLATECCCCCCCC
      CALL MOVEA(0.,300.)
      LA4='ALTERNATE ALPHA & TRANS PARAMETERS'
      CALL CHARTK(LA4,.9)
      WRITE(ZZ4,'(F7.4)')ALPHALT*57.2
      WRITE(ZZ5,'(F9.5)')TRANSQALT
      CHAR(13)=ZZ4//'     PtQ'//ZZ5
      CALL MOVEA(00.,275.)
      CALL CHARTK(CHAR(13),.9)
      IF(NFLAG.EQ.0)GO TO 6
      CALL MOVEA(-90.,230.)
      KA2='POINT  D(10*MM)  SX   SY   SZ   S(M/D)'
      CALL CHARTK(LA2,.900)
      DO 5 K-1,9
      CALL MOVEA(-60.,(225.-20*K))
      CALL CHARTK(CHAR(K),.750)
5     CONTINUE
6     CONTINUE
      CALL MOVEA(-300.,700.)
      CALL ANMODE
      PRINT '(''TICKLE VARIABLES'')'
      PRINT '(''TO END ENTER 9'')'
      WRITE( 1,103)TMAG
      WRITE( 1,104)GP
```

```
      WRITE( 1, 105)GQ
      TEMP10=TMAG
      TEMP11=GP
      TEMP12=GQ
      PRINT '(''ENTER NEW TMAG'')'
      READ(1,*)TMAG
      IF (TMAG.EQ.9)GO TO 10
      IF(TMAG.EQ.0)TMAG-TEMP10
      PRINT '(''ENTER NEW GP'')'
      READ(1,*)GP
      IF(GP.EQ.0)  GP=TEMP11' PRINT '(''ENTER NEW GQ'')'
      READ(1,*)GQ
      IF(GQ.EQ.0)GQ=TEMP12
      CALL RECOVR
      REWIND(5)
      READ(5,*)DUMMY
      CALL NEWPAG
      GO TO 9
103   FOMRAT('TMAG-',F9.5)
104   FORMAT('GAMMAP=',F9.5)
105   FORMAT('GAMMAGQ=',F9.5)
10    CALL ANMODE
      CLOSE(5)
      CLOSE(7)
      CALL CLOSTK(IER)
      END
```

BIBLIOGRAPHY

BIBLIOGRAPHY

1. LePichon, X., "Sea Floor Spreading and Continental Drift," J. Geophysical Res., 73, p3661-97, 1968.

2. Rasmussen, L., "Calculations of a Velocity Distribution from Particle Trajectory End-Points," J. Glaciology, 29, 102, p203-13, 1983.

3. Burch, J., and Tokarski, J. "Production of Multiple Beam Fringes from Photographic Scatterers," Optica Acta, 15, p101-11, 1967.

4. Archbold, J., Burch, J. and Ennos, A., "Recording of In-Plane Surface Displacement by Double Exposure Speckle Photography," Optica Acta, 17, p883-96, 1970.

5. Cloud, G., "Practical Speckle Interferometry for Measuring In-Plane Deformation," Applied Optics, 14, 4, p878-84, April, 1975.

6. Asundi, A. and Chiang, F., "Theory and Applications of the White-Light Speckle Method for Strain Analysis," Optical Engineering, 21, 4, p570-80, July-Aug., 1982.

7. Asundi, A. and Chiang, F., "Perspective Effect in the White-Light Speckle Method," Applied Optics-Letters, 21, 10, p1708-10, 1982.

8. Archbold, E. and Ennos, A., "Displacement Measurement from Double-Exposure Laser Photographs," Optica Acta, 19, p253-71, 1972.

9. Speckle Metrology, edited by R. Erf, Academic Press, New York, 1978.

10. Thompson, B., "Coherent Optical Processing-A Tutorial Review," Proc. Soc. Photo-optical Instrumentation Engineers (SPIE), 52, p1-22, San Diego, CA, Aug., 1974.

11. Boone, P. and DeBacker, L., "Speckle Methods Using Photography and Reconstruction in Incoherent Light," Optik, 44, 3, p343-55, 1976.

12. Burch, J. and Forno, C., "A High Sensitivity Moire Grid Technique for Studying Deformation in Large Objects," Optical Engineering, 14, 2, March-April, 1975.

13. Khetan, R. and Chiang, F., "Strain Analysis by One-Beam Laser Speckle Interferometry-1: Single Aperture Method," Applied Optics, 15, 9, p2205-15, September, 1976.

14. Maddux, G., "A Programmable Data Retrieval System for In-Plane Displacements from Speckle Photographs," Air Force Flight Dynamics Lab, Tech Report AFFDL-TM-78-109, Wright-Patterson AFB, Ohio, 1978.

15. Cloud, G. and others, "Feasibility of Non-Coherent Speckle Photography for In-Vivo Measurement of Skin Deformation," Proc. Optical Soc. of America Meeting on Holography and Speckle, Cape Cod, MA, May, 1980.

16. Cloud, G., "A New Whole-Field Interferometric Scheme for Measuring Surface Flow and Strain Rates in Glaciers," NSF grant No. CME-80-08273, 1979.

17. Miller, M., "Phenomena Associated with the Deformation of a Glacier Bore-Hole," Extrait Des Comptes Rendus et Rapports-Assemblee General de Toronto, International Union of Geodessy and Geophysics, Tome IV, p437-52, 1957.

18. Patterson, W., "Ice Sheets and Ice Shelves," Dynamics of Ice and Snow Masses, edited by S. Colbeck, U.S. Army Cold Regions Research and Engineering Laboratory, Hanover, NH, Academic Press, 1980.

19. Weertman, E., "A Mechanism for Continental Drift," J. Geophysical Res., 67, part 1, p1133-9, 1962.

20. Born, M., and Wolf, E., Principles of Optics, 3rd ed., Pergammon Press, NY, NY, 1973.

21. Ostrem, G., "ERTS Data in Glaciology-An Effort to Monitor Glacier Mass Balance from Satellite Imagery," J. Glaciology, 15, 73, p403, 1975.

22. Meier, M., "The Role of Snow and Ice in Hydrology; Properties and Processes of Glaciers," International Assoc. of Hydrological Sciences, 107, p353-70, 1972.

23. Ahlman, H., "Glacier Variations and Climate Fluctuations," Bowman Memorial Lectures-American Geographical Soc., New York, 1953.

24. Nye, J., "The Flow Law of Glaciers and Ice Sheets as a Problem in Plasticity," Proc. Royal Soc. A, 207, p554-72, 1952.

25. Glen, J. W., "Experiments on the Deformation of Ice," J. Glaciology, 2, p111-4, 1952.

26. Dyson, J., The World of Ice, Knopf, NY, NY, 1962.

27. Sherman, J., "Speckle Imaging Under Non-Isoplanatic Conditions," Proc. Soc. Photo-optical Instrumentation Engineers (SPIE), W. Carter ed., 243, p51-7, San Diego, CA, July, 1980.

28. Hodge, S., "Variations in the Sliding of a Temperate Glacier," J. Glaciology, 13, 69, p349-69, 1971.

29. Raymond, C., "Flow in a Transverse Section of Athabasca Glacier, Alberta, Canada," J. Glaciology, 10, 58, 1971.

30. Warner, G. "The Measurement of Surface Strain in Glaciers Using Embedded Resistance Gages," Ph.D. Dissertation, Michigan State University, 1973.

31. Warner, G. and Cloud, G., "Measurement of Surface Strain Rates in Glaciers Using Embedded Wire Strain Gages," Experimental Mechanics, 14, 1, p24, Jan., 1974.

32. Adams, F. and Maddux, G., "Dual Plate Speckle Photography," Tech. Report AFFDL-TM-75-57, AFFML, WPAFB, Ohio 45433, USA, 1975.

33. Nye, J., "The Flow of a Glacier in a Channel of Rectangular, Elliptic or Parabolic Cross-Section," J. Glaciology, 5, 41, p661-90, 1965.

34. Patterson, W., The Physics of Glaciers, Pergammon Press, Oxford, 1969.

35. Hutter, K., Theoretical Glaciology, Reidel Publishing Co., Dordrecth, Holland, 1983.

36. Raymond, C., "Temperate Valley Glaciers," Dynamics of Ice and Snow Masses, S. Colbeck, ed., Academic Press, London, 1980.

37. Welford, W., Aberrations of the Symmetrical Optical System, Academic Press, London, 1974.

38. Barnes, P. and others, "The Friction and Creep of Polycrystalline Ice," Proc. Royal Soc. A, 324, p127-55, 1971.

39. Labeyrie, A., "Attainment of Diffraction Limited Resolution in Large Telescopes by Fourier Analyzing Spectral Patterns in Star Images," Astron. and Astrophys., 6, 85, p85-7, 1970.

40. Claton, L. and Moran, S., "A Glacial Process-Form Model," Glacial Geomorphology, G. Coates, ed., Proc. 5th Annual Geomorphology Symposia Series, Binghamton, New York, Sept., 1974.

41. Dudderar, T. and Simpkins, P., "Scattered Light Speckle Metrology," Proc. Hologram Interferometry and Speckle Metrology, Optical Soc. of America, Cape Cod, MA, June, 1980.

42. Duffy, D., "Moire Gauging of In-Plane Displacement Using Double Aperture Imaging," Applied Optics, 11, 8, p1778-81, Aug., 1972.

43. Wu, T. and Christensen, R., "Measurement of Surface Strain Rates of the Taku Glacier, Alaska," J. Glaciology, 5, p305-13, 1966.

44. Chiang, F. and Li, D., "Diffraction Halo Functions of Coherent and Incoherent Random Speckle Patterns," Applied Optics, 24, 14, p2166-70, 1985.

45. Meynart, R., "Diffraction Halo in Speckle Photography," Applied Optics-Letters, 23, 14, p2235-6, 1984.

46. Gaskill, J., Linear Systems, Fourier Transforms & Optics, Wiley and Sons, NY, NY, 1978.

47. Goodman, J., Introduction to Fourier Optics, Holt, Rinehart and Winston, NY, NY, 1968.

48. Fowles, G., Introduction to Optics, Holt, Rinehart and Winston, NY, NY, 1968.

49. Meier, M., Kamb, W. and others, "Flow of Blue Glacier, Olympia Mountains, Washington, USA," J. Glaciology, 13, p187-212, 1974.

50. Duffieux, P., The Fourier Transform and Its Application to Optics-2nd Ed., Wiley and Songs, NY, NY, 1983.

51. Kauffman, G., "On the Numerical Processing of Speckle Photograph Fringes," Optics and Laser Technology, p207-9, August, 1982.

52. Vikram, C., and Vedam, K., "Processing Speckle Photography Fringes," Optics and Laser Technology, p207-9, August, 1982.

53. Worden, S., "High Angular Resolution Techniques: Speckle Interferometry and Related Methods," Proc. SPIE, Applications of Speckle Phenomena, W. Carter ed., p66-73, San Diego, CA, July, 1973.

54. Fried, D., "Optical Resolution Through a Randomly Inhomogeneous Medium for Very Long and Very Short Exposures," J. Opt. Soc. Am., 56, 10, p1372-9, Oct., 1966.

55. Korff, D., "Analysis of a Method for Obtaining Near-Diffraction-Limited Information in the Presence of Atmospheric Turbulence," J. Opt. Soc. Am., 63, 8, p971-80, Aug., 1973.

56. Korff, D., "Analysis of a Method for Obtaining Near-Diffraction-Limited Information in the Presence of Atmospheric Turbulence," reproducing the results of Hufnagel, J. Opt. Soc. Am., 63, 8, p974-5, Aug., 1973.

57. Von der Luhe, O., "Estimating Fried's Parameter from a Time Series of an Arbitrarily Resolved Object Images Through Atmospheric Turbulence, J. Opt. Soc. Am. A, 1, 5, p510-0, May, 1984.

58. Muirden, J., Astronomy for Amateurs, Cassell and Co., London, 1968.

59. Cloud, G., and Conley, E., "A Whole-Field Interferometric Scheme for Measuring Strain and Flow Rates of Glacier and Other Naturally Occurring Surfaces," J. Glaciology, 29, 103, p492-7, 1983.

60. Cloud, G., Conley, E. and Burgoon, E., "Whole-Field Interferometric Measurement of Strain and Flow Rates of Glacier and Other Naturally Occurring Surfaces," Proc. of the Ninth Canadian Congress of Applied Mechanics (CANCAM), Saskatoon, Saskatchewan, p927-8, May, 1983.

61. Conley, E. and Cloud, G., "Stereo Interferometric Measurement of Glacier Ice Strain Rates," Proc. Spring 1985 Conference of Soc. of Experimental Mechanics, Las Vegas, NV, p452-3, June, 1985.

62. Conley, E. and Cloud, G., "Whole-Field Measurement of Ice Displacement and Strain Rates," Proc. 5th International Offshore Mechanics and Arctic Engineering Symposium (OMAE), Tokyo, 4, p432-5, April, 1986.

63. Cloud, G. and others, "Noncoherent-Light Photography for Measurements of Fluid Velocity Fields," Proc. Soc. Photo-optical Instrumentation Engineers (SPIE), W. Carter, Ed., 243, p150-7, July, 1980.

64. Cloud, G., "Simple Optical Processing of Moire-grating Photographs," Experimental Mechanics, 20, 8, p265-71, August, 1980.